High rate and temperature-dependent tensile characterisation with modelling for gap-bridged remote laser welded (RLW) joint using automotive AA5182 alloy

Abhishek Das, Richard Beaumont, Ian Butterworth, Iain Masters, David Williams

WMG, The University of Warwick, Coventry, CV4 8GJ, United Kingdom

E-mail: A.Das.1@warwick.ac.uk

Abstract:

This paper investigates the high rate tensile behaviour of fillet edge joints produced by *'gap-bridged'* remote laser welding (RLW) using aluminium alloy AA5182. The RLW *'gap-bridged'* test specimens were produced considering three levels of the part-to-part gap; 0.0, 0.2, and 0.4 mm. Lap shear tests were performed to evaluate the high rate sensitivity in the test speed range from moderate (0.1 m/s) to high-speed rate (10 m/s) at room temperature (~23°C). This equates to a strain rate range from moderate (~ 10 s^{-1}) to near 1000 s^{-1}. Strain rate dependency was found to be low, however, an increase in tensile extension to failure was observed with increasing strain rate. Additionally, the effects of depressed (-50°C) to elevated temperatures (up to 300°C) on the joint tensile performance were evaluated. Fracture strain was computed at room temperature using the digital image correlation (DIC) method and the fracture strain across the weld area was in the range from 0.140 to 0.194 for all the gap and speed conditions. This paper compares the RLW experimental test results with finite element modelling for industrial use. To evaluate joint performance, the lap shear strength of RLW samples was also compared with self-piercing riveting and resistance spot welding.

Keywords: High rate tensile performance; Remote laser welding; Fillet edge weld; Strain distribution; Fracture strain; Finite element model

1. Introduction

Due to strict legislation on the emission of greenhouse gases [1, 2], automotive manufacturers are moving towards improved fuel economy or electrification of vehicle powertrains [3]. Both

strategies need lighter body-in-white (BIW) structures which can be achieved by considering the use of lightweight materials, e.g. aluminium alloys with a higher strength-to-weight ratio [4, 5]. Aluminium alloys are already extensively used in transportation to build body-in-white structures and closure panels, aerospace fuselages, railway carriages etc. Additionally, aluminium alloys are also being used for electric vehicle battery enclosure/housing as well as battery interconnect joining [6-8]. Using aluminium intensive space frames, automotive body weights can be reduced by up to 50% [9] in comparison with conventional steel body structures. In addition, automotive closure/skin panels including hoods, doors, wings and bumpers benefit from the use of aluminium alloys due to their good formability, enhanced corrosion resistance and potential recyclability [4]. The 5xxx aluminium alloy series (i.e. Al-Mg-Mn alloys), are insensitive to heat-treatment which makes it attractive for both hot and cold rolled sheet production and they are largely used in Europe for automotive closure panels due to their good formability, high strength and strain hardening capability [9]. In general, AA5xxx series alloys are extensively being used for structural and skin panel applications in automotive body-in-white. A popular high magnesium content alloy (>4% Mg), AA5182, is generally used where high strength and complex shape formation is required especially for structural applications.

In general, complex structures often require a number of parts to be joined to produce a successful functional component. Welded joints are preferable as they are fast to produce, flexible to place and cost effective. However, making welded joints with aluminium alloy is not trivial, due to the presence of oxide layers, its high thermal expansion coefficient and high thermal conductivity [10, 11]. Several joining methods have been successfully adapted to join aluminium sheet metal parts including resistance spot welding (RSW) [12, 13], self-piercing riveting (SPR) [14, 15], friction stir welding (FSW) [16, 17], and laser welding [18, 19]. A variant of laser welding, remote laser welding (RLW), is emerging as a new joining technique across sheet metal industries, especially in automotive and aerospace lightweight material

joining applications, due to its potential to reduce cycle time, floor space, and cost [20]. For automotive body-in-white or closure panel joining, RLW can replace self-piercing riveting and resistance spot welding by reducing weight and energy consumption respectively [18]. However, the main challenge to produce a satisfactory weld using RLW is to ensure tight part-to-part fit-ups/gaps [21, 22]. Part-to-part gaps are common occurrences during assembly operations for numerous reasons including part stamping springback [23-25], geometric/shape errors [26, 27], part location errors [28], improper fixture design [21, 29] which result in improper part-to-part surface fits [22, 30]. A number of corrective and preventive actions can be taken to mitigate the part-to-part gaps during the assembly process starting from part production with tight tolerances [31], fixture optimisation [21, 32] and gap-bridging during welding operation [33, 34]. One of the proven ways to close the part-to-part gaps is by employing seam tracking based laser triangulation to determine the gap height between the sheets, setting angles of the optics in reference to the workpiece [33], and then performing beam oscillation and/or beam defocusing to bridge the part-to-part gaps [35].Therefore, the novel '*RLW gap bridging*' technique [33, 35] offers an effective joining technique which can accommodate part-to-part gaps in fillet edge joint configuration [18, 34]. Figure 1 shows typical joints of the two sheets (a) without gap and (b) with a part-to-part gap condition.

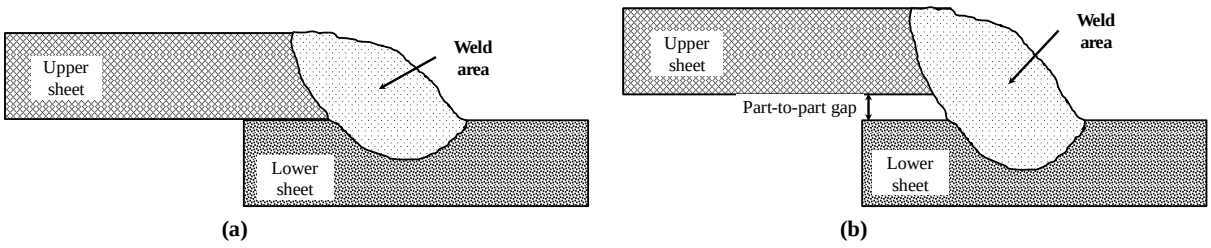

Figure 1 RLW fillet edge weld configurations (a) without, and (b) with part-to-part gap [18].

Being a newly developed technique, joints produced by *RLW gap bridging* need to be evaluated in terms of joint performance by comparing with current industrial techniques. Recent attempts have been reported to evaluate the feasibility of RLW gap bridging for both steel and

aluminium joints [33]. However, they are mainly limited to the basic understanding of joint microstructure and tensile properties [18, 36]. This basic evaluation is not sufficient for automotive applications where understanding joint performance during crash events is essential [5]. High rate tensile performance of gap-bridged joints is therefore required, but the authors are unaware of this being reported in the literature.

1.1. *Review of high rate characterisation*

In general, aluminium and its alloys are considered to have low strain rate sensitivity [37, 38]. The available literature on high strain rate characterisation is mainly restricted to the parent material. Reported studies on the strain rate sensitivity consider various aluminium alloys including AA2124 [39], AA5052 [40], AA5182 [41, 42], AA5754 [43], AA6026 [44], AA6082 [37], AA7018 [37] and AA7075 [45]. In addition, special attention was given to 5xxx series aluminium alloys for high rate forming applications [46] to develop automotive components, such as inner panels and body-in-white components [4]. As 5xxx series contains a high percentage of Mg, Mukai, et al. [47] performed tensile tests on the high purity Al-Mg alloys with magnesium concentration increasing from 1.8 to 8.4 wt% and a transition from negative to positive rate sensitivity was observed at strain rates of 10 -100 s^{-1}. Higashi, et al. [48] examined strain rate performances of AA5182 parent material in between 1×10^{-3} and 4×10^{3} s^{-1} at ambient temperature. In general, the maximum flow stress decreased with increasing strain rates and material elongation to failure increased with strain rates. Smerd, et al. [5] extended the high strain rate tensile testing by adapted Johnson-Cook constitutive model to fit AA5182 aluminium alloy sheet and they have concluded that the rate dependency of flow stress was low. Further investigations have been conducted in different material directions (rolling direction, 45° to the rolling direction, and transverse direction) at strain rates ranging from 0.001 to 1000 s^{-1} and compared different constitutive models using genetic algorithm and neural network [42]. Additionally, Rahmaan, et al. [41] conducted shear tests at varying strain

rates using AA5182-O aluminium alloy sheet at room temperature. Only limited sensitivity on strain rate was observed. The work reported on AA5182 aluminium alloy has been limited to parent material testing rather than the joint performance testing and consequently, it is necessary to evaluate the joint performance at high rate tensile testing.

1.2. *Review of depressed and elevated temperature characterisation*

Similar to high strain rate characterisation, limited studies are reported in the literature on depressed and elevated temperature characterisation and they are not focused on joint characterisation. One of the emerging applications for aluminium sheet metal and subsequent laser welded joints are battery casings/housings for electric vehicles (EVs) which contain large numbers of cells [3, 6]. Battery casings and their integral laser welded joints can be subjected to extremes of temperature for example during a battery fire (i.e. thermal runaway) or during cryogenic transport [49, 50]. It is therefore of interest to understand how the welded joints behave over a range of temperatures. Most other studies have focused on parent material thermal softening rather than the joint characterisation. For example, to understand the performance of aluminium alloys during a fire, Summers, et al. [51] reported high temperature quasi-static mechanical behaviour of 5083-H116 and 6061-T651 where a gradual decrease in ultimate strength was measured with higher temperature. When AA7017 aluminium alloy was tested from room temperature to 300 °C, Bobbili, et al. [52] confirmed that the flow stress decreases with an increase in temperature and beyond 200 °C the deformation mode is largely affected by thermal softening. In a similar study, parent material uniaxial tensile tests were conducted on AA5182-O at temperature levels of 25, 100, 200 and 300 °C using slow to moderate strain rates [53] and flow stress was found to decrease with the increase of temperature. However, the aforesaid characterisation is basically focused on parent material testing at elevated temperatures. There is a need to characterise joints themselves at depressed and elevated temperatures.

1.3. *Research gap and objectives*

Metallographic characterisation and the low rate tensile performance are reported in the literature for various steel and aluminium based laser joining applications [18, 19, 54]. However, the high rate tensile characterisation was mainly performed on steel laser joints in a bead-on-plate or butt joint configuration. Liu, et al. [55] studied laser welded commercial grade DP780 steel in butt configuration for high rate characterisation where laser welding was conducted using a pulsed Nd:YAG laser system (LWY-500) with a maximum mean power of 500 W. They also reported the use of digital image correlation (DIC) and high-speed photography based analyses for the strain measurement of the DP780 welded joints during dynamic tensile tests. Similarly, Dong, et al. [56] and Jia, et al. [57] reported strain rate dependent behaviour of butt welded DP600 and DP980 steels, respectively. These are laser welded bead-on-plate or butt configuration using mainly dual phase steels. However, high-speed tensile characterisation of laser welded joints using aluminium alloy is missing from the literature. Additionally, tensile responses from RLW fillet edge welds under depressed and elevated temperatures are also not reported in the literature.

The typical joint configuration for two sheets using the RLW gap bridging technique is the fillet edge weld type (refer to Figure 1). Therefore, this has been considered for the high rate characterisation study. This paper addresses the aforesaid research gap by determining the following: (1) evaluation of the high-speed tensile performance of gap-bridged fillet edge joints and understanding the tensile performance under depressed and elevated temperatures, (2) strain mapping and measurement using digital image correlation, (3) finite element model development to predict the joint behaviour, and (4) comparison of RLW gap-bridged joints with industrial joining processes, such as resistance spot welding (RSW) and self-piercing riveting (SPR).

2. Materials and methods

2.1. Details of Substrate Material

The as-received AA5182 – H111 aluminium alloy sheets of 1.0 mm nominal thickness and chemical composition (wt %) of Al-4.5Mg-0.34Mn-0.35Fe-0.2Si, were assembled by overlapping 25 mm to produce the RLW gap bridged fillet edge weld. The detailed parent assembly preparation, aluminium sheet cleaning and tensile sample preparation are reported in Das, et al. [18]. From the parent assembly, tensile samples of 29 mm in width were prepared as adapted from BS EN ISO 26203-2 [58] and Wood, et al. [59]. The physical and mechanical properties of AA5182 alloy are reported in Table 1.

Table 1 Physical and mechanical properties of AA5182 alloy used in this study for the joint modelling and simulation [16, 60, 61].

Properties	Alloy Grade AA5182 – H111
Density [10^3 kg/m^3]	2.7
Young's modulus, E (GPa)	69
Shear modulus (GPa)	26
Yield strength (0.2%) [MPa]	129
Tensile Strength, UTS (MPa)	280
Strength Coefficient, K (MPa)	582
Poisson's ratio	0.31

2.2. RLW gap-bridging experimental details

The fillet edge welds for the high rate characterisation were produced using a Scansonic Remote Laser Welding-Automatic (RLW-A) optical head with a maximum power of 5.0 kW and an IR wavelength of 1030 nm. The nominal focal distance was 500 mm with a nominal spot size of 580 µm when the laser was delivered by a fibre of 200 µm in diameter. Two identical AA5182 aluminium sheets with dimensions of 450 mm × 175 mm were assembled to

produce the parent assembly overlapping 25 mm of the upper part on the lower part on their long edges [18]. A schematic illustration of the fillet edge weld specimen is shown in Figure 2. The RLW-A optical head was mounted on a KUKA VKRC 150 robot and as remote laser welding is an autogenous process, no filler wire or shield gas was used during the welding. As the welding head is positioned away from the target, a long focal length is required to focus the laser beam. To achieve a high welding speed, a fast beam movement was necessary [62] making it difficult to provide effective gas shielding over the large welding area. However, both Müller, et al. [35] and Weller, et al. [63] have demonstrated that aluminium can be successfully welded using RLW without shielding gas, and laser equipment manufacturers are now developing the RLW process without the provision for shielding gas supply. Additionally, this study has demonstrated that good quality RLW fillet edge welds can be produced without the need for shielding gas.

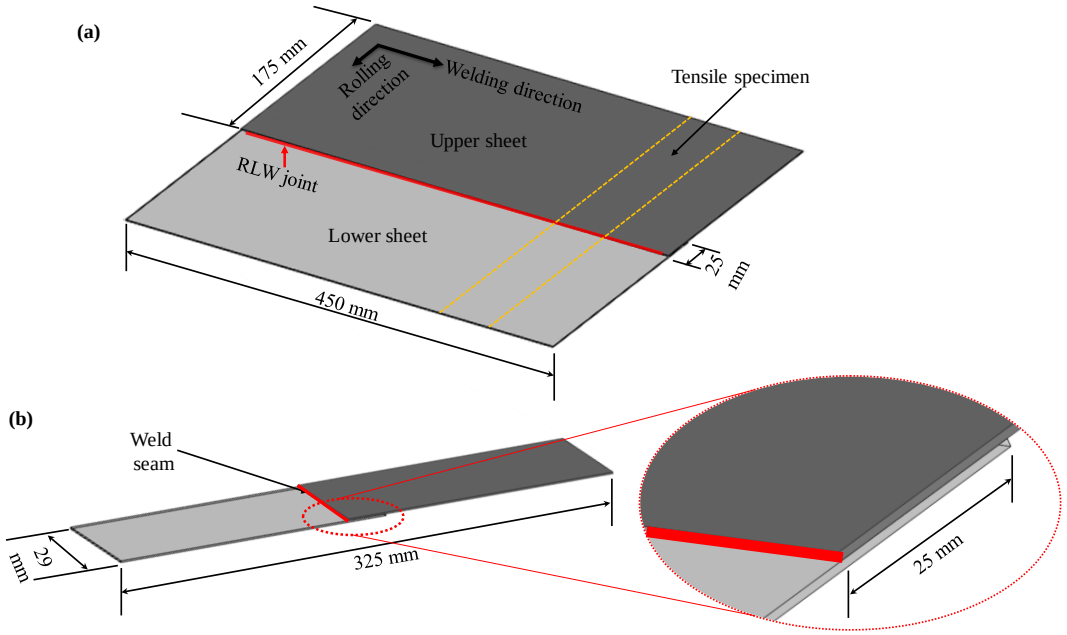

Figure 2 Schematic illustration of RLW fillet edge weld samples for high rate characterisation (a) dimensions of parent assembly and sample positions of tensile specimens, and (b) tensile specimens for high rate characterisation [18, 64].

It has been reported in the literature that the commonly investigated gaps are zero, 0.2 mm, and 0.4 mm gaps [65-67]. These gap values were chosen for the high rate tensile characterisation as they are production representative gap values. Initial screening tests were performed to map feasible ranges of laser process parameters to produce satisfactory fillet edge welds. Relying on these pilot tests and part-to-part gaps, the laser welding parameters were chosen and they are listed in Table 2. It can be observed that laser power was increased with the part-to-part gap which was essential to bridge the gaps as additional material from the upper part was required to be melted and fused with the lower part.

Table 2 RLW process parameter used to produce fillet edge welds at different part-to-part gaps

Sl No	Part-to-part gap [mm]	Laser Power [kW]	Welding Speed [m/min]
1	0.0	2.1	4.0
2	0.2	2.4	4.0
3	0.4	2.7	4.0

2.3. Details of high rate test conditions

Typically for automotive applications, materials were tested over a range of high rates as recommended in ESIS [68], Wood, et al. [59]. An Instron – Very high rate testing machine (Instron precision servo-hydraulic VHS 160/100-20), having controlled velocity in the range 10 mm/s to 20 m/s and rated to a maximum impact force of 100 kN, was utilised for this high rate tensile characterisation. For high rate testing, a moving jaw was used to grip the upper side of the tensile specimen at the designed position after it has attained its target speed. The moving jaw set-up was connected to a hydraulic actuator, the movement of which was measured using a displacement transducer. The grip displacement was therefore determined directly from the actuator movement. Wood, et al. [59] confirmed that the relative displacement between the actuator and the grip was so small that they could be considered identical when compared to

the displacement of the specimen. The static grip head is attached to a dynamic load cell (DLC) to measure force using a piezo type load washer, located at the base of the machine platform. The span between static and moving grips when the specimen was gripped was 225 mm.

The RLW gap bridged fillet edge welds were tested over the speed range from moderate (0.1 m/s) to high rate (10 m/s) as recommended by Wood, et al. [59]. Additionally, Wood, et al. [64] tested self-piercing riveted aluminium joints at speeds of 1.0 mm/s to 5.0 m/s. Similarly, Liu, et al. [55] conducted high rate dynamic tensile tests at 0.1, 1.0, 5.0 and 10.0 m/s. Based on the recommendations and previous work reported in the literature, three repeats were performed for the test speeds of 0.1 m/s, 1.0 m/s, 5.0 m/s and 10.0 m/s on test specimens produced with different part-to-part gap values.

The Instron test frame was fitted with a thermal chamber which operates between -50 °C to 350 °C. The temperature can be controlled using the in-built thermocouple and an additional thermocouple was attached to the static side of the test sample for accurate measurement of sample temperature rather than the ambient air temperature. Apart from the abovementioned high-speed testing at room temperature (~23°C), the joint tensile performance was evaluated at -50°C, 0°C, 50°C, 100°C, 200°C, and 300°C. To identify the effects of depressed and elevated temperatures, all the tests were performed at 0.1 m/s in order to minimise the noise in the test data. As the thermal chamber needed to be placed below the upper grip, a total specimen length of 525 mm (i.e. 450 mm × 175 mm were assembled with 450 mm × 375 mm to produce the assembly by overlapping 25 mm of the upper part on the lower part on their long edges) was required. Then, larger samples of 525 mm × 29 mm were obtained from the assembly for temperature based joint strength characterisation. Therefore, the span between static and moving grips when gripping the specimen was 425 mm. The depressed temperatures (i.e. -50°C and 0°C) were obtained using liquid nitrogen whereas the elevated temperatures were attained using the in-built heating coil within the thermal chamber.

To capture the strain development at various test speeds, dynamic strain measurement was performed using a full-field strain measuring system (i.e. GOM Aramis platform) based on the digital image correlation (DIC) method [69] where the images were captured using a non-contact Photron FASTCAM SA-X2 monochrome camera at the four representative test rates of 0.1, 1.0, 5.0, and 10.0 m/s. In order to capture the strain occurring during the tests, the tensile samples were first painted matt black over which a random dotted white speckle pattern was applied. High-speed photography was utilised to capture the relative movement of these speckles to study the deformation process of the specimens up to fracture. The camera lens was positioned perpendicular to the joint surface at a distance of 800 mm from the sample to ensure the field of view covered the full elongation of the test specimen (see Figure 3). Additional external light was utilised to illuminate the investigated speckle pattern surface for easy capture of their relative movement. In this study, frame rates of 1000, 20000, 50000, and 80000 frames per second (fps) were used from the start of the tensile tests until fracture occurred for the test speeds of 0.1, 1.0, 5.0, and 10.0 m/s, respectively. Typically, an increase in frame rate has a detrimental effect on the frame resolution. Therefore, the same resolution cannot be used for both slow and high speed tests. Based on the moderate number of images required to capture the strain distribution, the image size in pixels was reduced over the range of speeds as follows 1024 × 1024, 1024 × 1024, 384 × 560 and 384 × 336 for the test speeds of 0.1, 1.0, 5.0, and 10.0 m/s respectively. In each image, the length/pixel was 0.105 mm. Therefore, larger areas were covered by the images at the lower speeds whereas specific areas of interest in the samples were covered at higher speeds. The number of images was dependent on the test speed, as the duration of the dynamic tensile test is inversely proportional to the test speed.

The GOM ARAMIS DIC system uses a random speckle pattern applied to the surface of the target object to create the unique features identifiable to the system. To identify these features

each image was divided into a grid of facets and each facet must be unique from its neighbouring facets. The facet (also known as subset size), step size and strain filter window were 15×15 pixels, 13 pixels and 3×3, respectively. The strain calculation was done based on lowest possible 3×3 field of data points which was suitable for the assessment of local strain [70]. These facets were distributed within the average masked area of 35 × 25 mm.

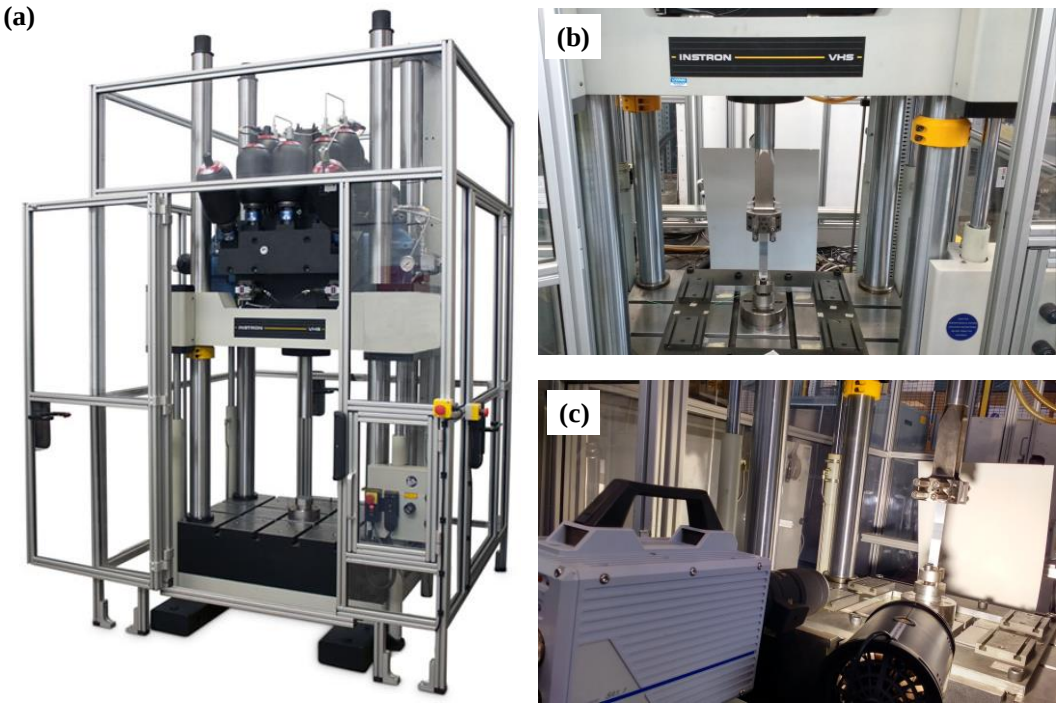

Figure 3 (a) Instron – Very high rate testing machine, Instron precision servo-hydraulic VHS 160/100-20 (adapted from Instron), (b) RLW specimen set-up for high rate testing, and (c) dynamic strain measurement using a non-contact Photron FASTCAM SA-X2 monochrome high-speed camera.

3. Results and discussion

3.1. Load-Displacement responses and mechanical properties

3.1.1. Base material and fusion zone

To evaluate the base material properties, tensile tests were performed using an Instron 5800 test frame with a 100 kN load capacity and an axial video extensometer was used to measure axial tensile strain. The tensile specimens of 40 mm gauge length were used to obtain the stress-

strain curve of base material using a static test speed of 2 mm/min. Three tests were performed to evaluate the stress-strain behaviour, and further, these results were used for the lap shear FE modelling. Figure 4(a) describes the engineering stress-strain curves of the AA5182 base material. The measured average 0.2% proof stress, maximum tensile stress (i.e. ultimate tensile strength), maximum load and tensile extension at maximum load were 128.8 MPa, 282.14 MPa, 2866.63 N and 9.44 mm, respectively. The calculated Young's modulus was 68.89 GPa. Furthermore, these base material properties are utilised for the rate characterisation and subsequent FE modelling.

Detailed RLW gap bridging principle was explained in [18], and good weld quality was considered when penetration depth remained in between 0.2 to 0.7 times of the lower sheet thickness. The effects of laser process parameters (i.e. laser power and welding speed) on the key geometric features (such as penetration depth and leg length – as shown in Figure 4) were explained in details by Das, et al. [18]. Relying on characterisation, only welds with satisfactory weld quality were chosen in this study for high speed tensile and temperature-dependent characterisation. The cross-sectional images of the zero gap, 0.2 mm and 0.4 mm part-to-part gap bridged fillet edge welds are shown in Figure 4(b) – (d). Penetration depths of 457.15 µm, 410.05 µm, and 395.4 µm were obtained from zero gap, 0.2 mm and 0.4 mm part-to-part gaps respectively which confirmed their classification as good-weld and suitable for further characterisation in this study. Similarly, the leg length values were 1434 µm, 1450 µm, and 1570 µm for zero, 0.2 mm and 0.4 mm part-to-part gap-bridged fillet edge welds, respectively.

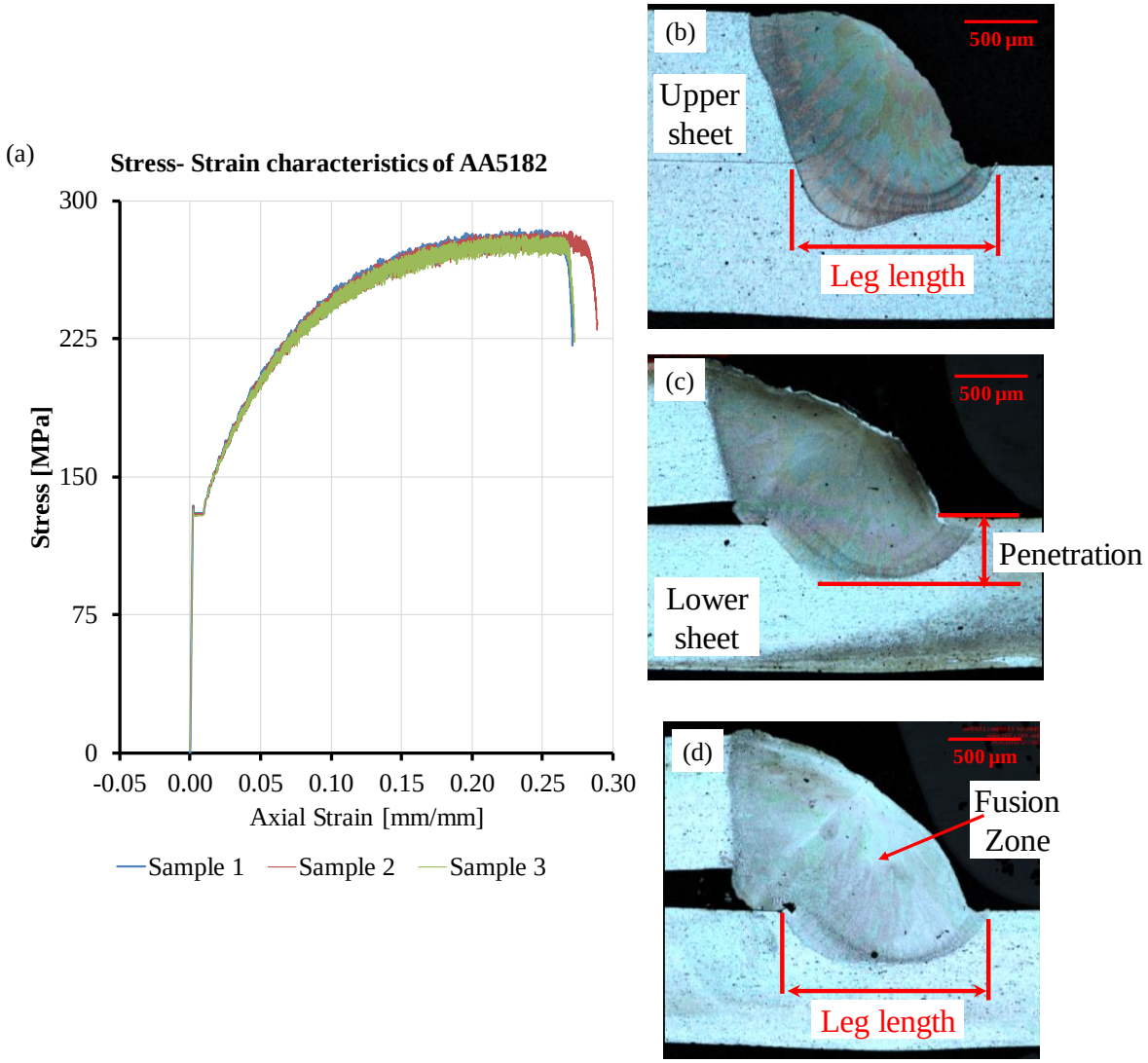

Figure 4 (a) Stress-strain behaviour of AA5182 base material, and (b) – (d) represent the cross-sectional images of fusion zone obtained from zero gap, 0.2 mm and 0.4 mm gap-bridged RLW fillet edge welds, respectively.

3.1.2. High-speed tests of RLW fillet edge weld

Three specimens were tested for each part-to-part gap condition (i.e. 0.0 mm, 0.2 mm and 0.4 mm gaps) at four dynamic test speeds (i.e. 0.1, 1.0, 5.0 and 10.0 m/s). Obtaining the actual cross-sectional area of the gap-bridged laser seam is difficult as there is localised variation in the fusion zone contact region, so the load-displacement curves [18] are preferred for the welded joint strength evaluation and its responses for high rate tests. High-speed test results have a high value of noise due to inertia effects of the system [64]. Therefore, a two stage

299 filtering process was employed to enable the determination of maximum force and grip
300 displacement. Firstly, a Butterworth filter with 1 kHz cut-off frequency to get rid of high
301 frequency noise in the data and then a moving average filter to smooth the low frequency noise.
302 For example, the unfiltered and filtered tensile test results are plotted in Figure 5(a) when a
303 zero gap fillet edge weld was tested at 5.0 m/s and 10.0 m/s. By applying the filtering process,
304 Figure 5(b) reports the load-displacement curves obtained from the three repeat tests of zero
305 gap fillet edge weld at 1.0 m/s. The average load-displacement behaviour was obtained from
306 these tests and further applied to all speed and part-to-part gap conditions. The average load-
307 displacement curves obtained from different moderate to high tensile test rates are plotted in
308 Figure 6.

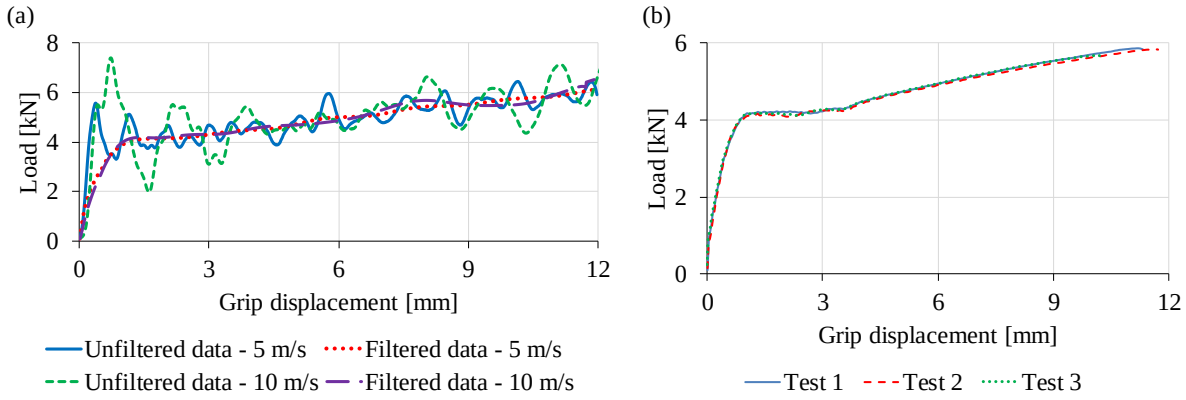

309

310 Figure 5 (a) Unfiltered and filtered load-displacement curves from zero gap fillet edge weld
311 test at 5.0 m/s and 10.0 m/s, and (b) load-displacement curves obtained from the repeat tests of
312 zero gap fillet edge welds at 1.0 m/s.

313 Maximum mean load and maximum mean grip displacement to failure were considered as the
314 weld performance measures for high rate characterisation. These values are shown in Figure
315 6(d) with associated standard errors. It was observed that the test speed had little effect on the
316 mean load at failure whereas the mean grip displacement at failure was increased with test
317 speed. Rusinek and Rodríguez-Martínez [38] reported similar low strain rate sensitivity when
318 they used Al-Mg alloy, and additionally, Wood, et al. [64] showed low strain rate sensitivity

when they joined AA5754 alloy sheets with self-piercing riveting tested over a rate from low rate (10^{-3} m/s) to high rate (5.0 m/s). However, in the case of RLW gap-bridged fillet edge welds, a small increment in load was observed with increasing rate of tests together with increment in mean grip displacement at failure. For example, in the case of zero gap based fillet edge weld tests at different test rates, an incremental 4 – 6 % change in maximum load at failure was observed. In contrast, a maximum of 20 – 30% increase in mean grip displacement at failure was observed when test speed was increased from 0.1 m/s to 1.0 m/s for all gap conditions. Thereafter, only a small increment was obtained in the mean grip displacement at failure when the test speed was increased from 1.0 m/s to 10.0 m/s. This phenomenon can be attributed to the change in flow stress, dynamic recovery or adiabatic heating effect at higher strain rates [71, 72]. Furthermore, it was observed that both the average mean load at failure and average grip displacement at failure decreased with increasing part-to-part gap values. In general, it is expected that increasing part-to-part gap results in weaker joints since the size of the fusion zone having overall good contact area with the low base material is reducing as well as lower penetration values being achieved with higher gaps [18]. This phenomenon was reflected with lower load values obtained from different part-to-part gap conditions.

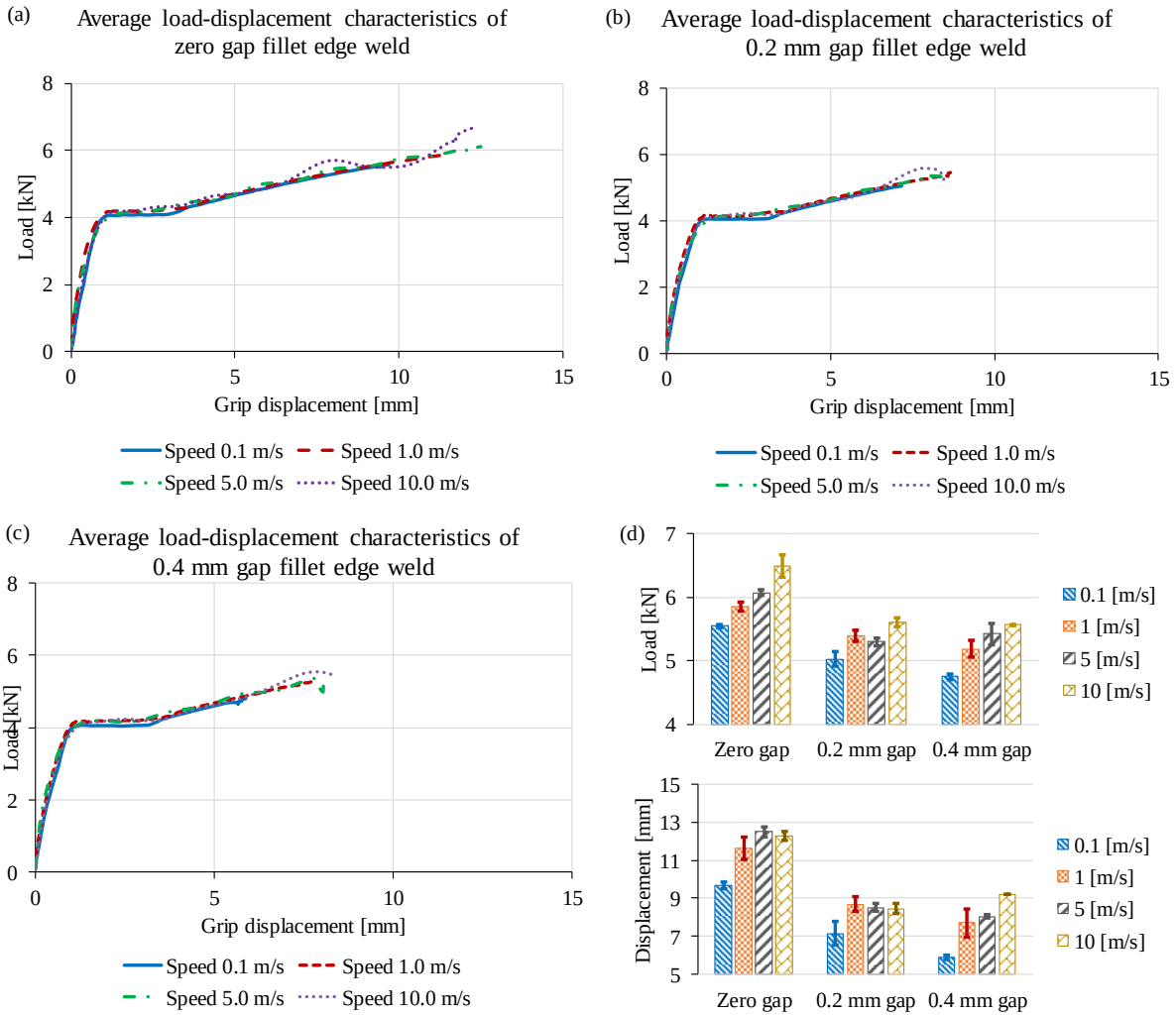

Figure 6 Load-displacement curves from lap shear tests of fillet edge welds at room temperature (~23°C) and various test speeds (a) zero gap, (b) 0.2 mm gap, (c) 0.4 mm gap, and (d) maximum mean load and corresponding mean displacements for the different speed and gap conditions with associated standard deviations.

3.1.3. Effects of depressed and elevated temperatures

Similar to previous tests, three tests were performed for the three part-to-part gap conditions (i.e. 0.0 mm, 0.2 mm and 0.4 mm gaps) at six levels of the temperature of which two were at depressed temperature (i.e. -50°C and 0°C) and other four at elevated temperature (i.e. 50°C, 100°C, 200°C, and 300°C). The average load-displacement curves obtained from all three gap-bridged RLW fillet welds at varying temperatures are plotted in Figure 7(a)-(c). The average

load and corresponding displacement obtained from the test conditions are shown in Figure 7(d) with their associated standard deviations.

In general, it was observed that load-displacement characteristics remain almost the same in-between -50°C and 100°C, however, the failure points were decreased with increasing temperature. It was noticed that tensile strength and elongation at failure points were highest at -50°C for all the part-to-part gap conditions. In general, aluminium alloys exhibit higher strength, ductility and fracture toughness at depressed temperatures by a significant improvement in strain hardening behaviour [73]. In the case of zero gap RLW fillet edge weld as in Figure 7(a), it can be observed that highest load of 6.09 kN was obtained at failure with largest grip displacement of 22.03 mm. With an increase in temperature, both the maximum load at failure and corresponding displacement gradually reduced without a significant reduction in yield point strength up to 100°C. For example, gradual decreasing average load of 5.83 kN, 5.51 kN and 5.32 kN were recorded at grip displacement of 19.82 mm, 16.22 mm and 14.87 mm when zero gap RLW fillet edge weld samples were tested at 0°C, 50°C and 100°C respectively. Similar load-displacement behaviours were obtained from 0.2 mm and 0.4 mm gap bridged RLW fillet edge welds as shown in Figure 7(a) and (b) respectively. However, gradual loss of yield strength was observed beyond 200°C, similar to maximum load and displacement at failure, as the flow stress was considerably decreased with the increase in temperature [53]. This mechanical property degradation at elevated temperature can in part be understood through the strengthening mechanisms. Langhelle and Amdahl [74] observed that the initial degradation occurred at a temperature as low as 150 °C with an additional 50% loss in yield strength at ~275 °C. A similar observation was reported by Summers, et al. [51] when 5083-H116 aluminium alloy was tested between 200°C – 350°C. In general, 5xxx series alloys are strain hardened and predominantly attain strength through grain refinement. Fine grains restrict the movement of dislocations resulting in increased strength [75]. At lower temperature

(150–250 °C), a partial loss of strength occurs due to subgrain coarsening and dilution of the Mg solid solution content in the aluminum matrix [76]. In contrast, at higher elevated temperatures (250-350 °C), the primary reduction in strength is caused by recrystallization upon annealing, a process which destroys grain refinement. Therefore, gradual loss of yield strength was observed beyond 200°C, accompanied by a reduction in maximum load, as the flow stress was considerably decreased with the increase in temperature [51, 53]. At the temperatures of 200°C and 300°C, yield strength of 3.6 kN and 2.9 kN was observed from all the three gap-bridged fillet edge weld samples. In case of 0.2 mm gap-bridged RLW fillet edge weld, approximately 40% decrease in grip displacement was observed when the temperature was raised from 100°C to 200°C or 200°C to 300°C whereas 12% and 17% reduction in maximum load at failure was observed. When comparing the maximum load and grip displacement at failure across part-to-part gap conditions, similar behaviour was obtained from all the tests with only small variations which can be attributed to laser welding variability as different power levels were used to bridge the gaps.

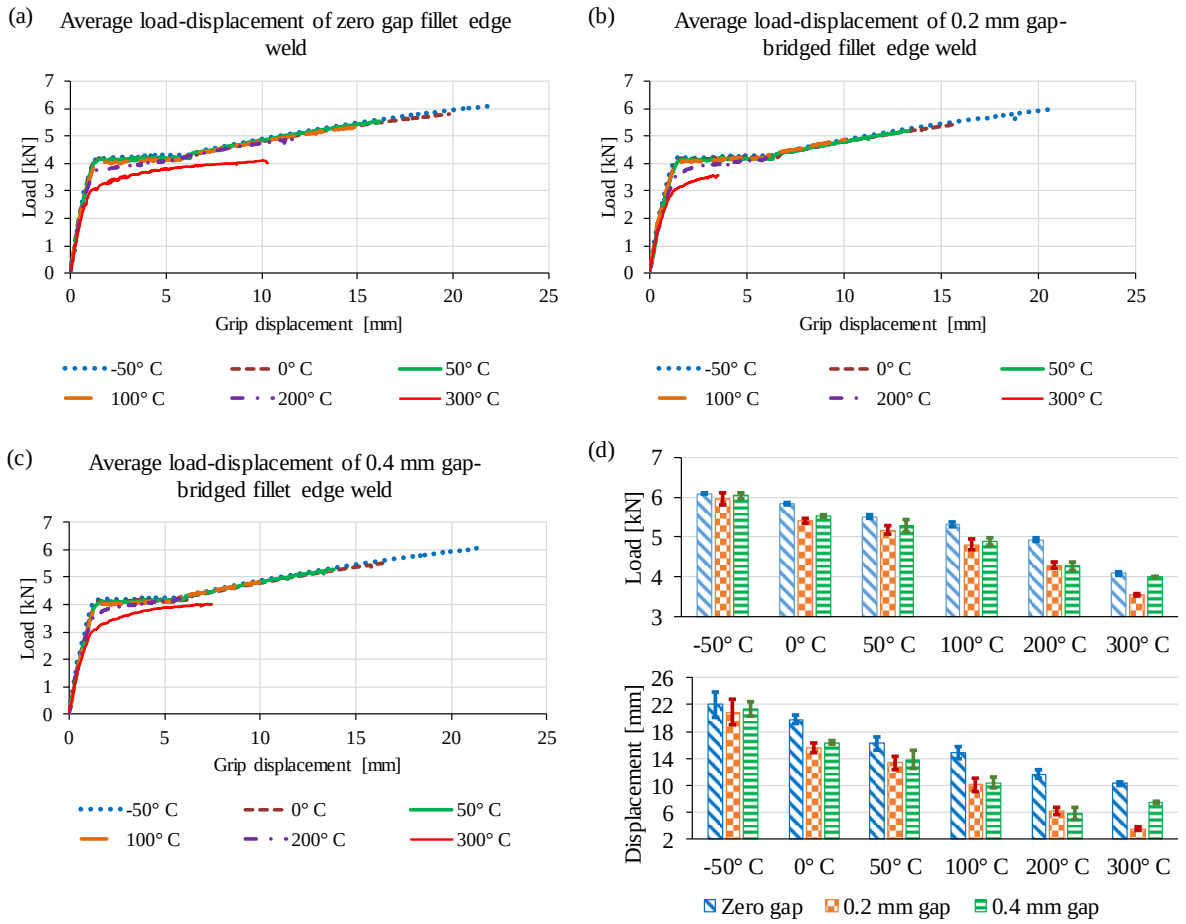

Figure 7 Load-displacement characteristics at depressed and elevated temperatures for fillet edge welds at (a) zero gap, (b) 0.2 mm gap, (c) 0.4 mm gap, and (d) maximum mean load and corresponding mean displacements to failure with associated standard deviations.

3.2. Strain distribution using DIC method

DIC based strain distribution measurement [69] at various tensile rates provides information about the deformation process and local strain distribution near the weld area [55]. The axial deformation with selected image sequences of strain mapping obtained from DIC for the 0.2 mm RLW gap-bridged joint at the tensile rates of 0.1, 1.0, 5.0 and 10.0 m/s are shown in Figure 8. The aspect of axial deformation and axial strain across the weld region was computed by assigning a local gauge length of 4.08 mm across the weld region at the start of loading. This local gauge length was selected based on the major strain development across the weld zone. Thereafter, the change in the local gauge length was analysed and reported as an axial strain vs

time distribution curve. These axial strain vs time curves can be divided into three distinct regions, namely, an initial linear elastic region, a plastic plateau as the material yields followed by a region of increasing stress as the material strain hardens. The axial strain corresponding to elastic region was related to the elastic behaviour of the test specimen before the proportional limit/elastic limit whereas the yielding behaviour was captured in the axial strain corresponding to plastic plateau. Subsequent axial strain with increasing stress corresponded to the strain hardening region.

It was observed that the specimen initially deformed uniformly upon loading but shortly after, strain localisation started to appear. This phenomenon can be attributed to the nature of the lap shear sample as the deformation was not symmetric. The lower overlap part was bent away from the upper part making the fusion zone act as a hinge point where the strain started to localise. With the increase in grip displacement, the measured load and subsequent elongation within the fusion zone were increased. Elongation of the fusion zone accompanied with slight rotation resulted in the lower overlap part bending. These non-symmetric modes of deformation and failure were consistent for all the lap shear specimens tested at all speeds and all part-to-part gaps. The fusion zone was observed to be weaker than the base material [18] and the location of the failure generally occurred within the welded region near to the upper base material. For example, take the results from the 0.2 mm gap-bridged fillet edge weld test at 1.0 m/s (Figure 8(c)), it can be seen from the stage images that the specimen had strain localisation at 2 ms when it was still within the plastic plateau region. In fact, the strain localisation was observed at quite an early stage of the elastic region due to aforesaid asymmetric deformation as well as weaker joint area compared to the base material. Typically, the axial strain development curve was started by increasing loading with strain localisation at the joint and elastic extension of the overall specimen and finally ended with localised abrupt facture /peeling along the joint seam. It was also observed that the length of the axial strain

corresponding to plastic plateau region was decreasing with the increased tensile test rate due to the coupled effects of high speed and simultaneous material deformation response rate at the plastic plateau and plastic increment region. Typically, the major difference in mechanical behaviour between static and dynamic tests can be attributed to the activation of different slip systems, differences in dislocation mobility, pile up and accommodation processes under different strain rates [77]. Gurrutxaga-Lerma, et al. [78] studied the mechanisms governing the activation of dislocation sources in aluminium at different strain rates. They found that the strain rate had a direct influence on the activation time of dislocation sources. At higher test speeds, early activation of the motion of the dislocation accompanied by higher deformation rate had resulted in a shorter plastic plateau region, and subsequently, larger mean grip displacement and maximum load at failure. Similarly, axial deformation measurements for different gap based fillet edge welds at 1.0 m/s with selected sequences of strain mapping are shown in Figure 9. Therefore, by adapting this approach, the axial strain development curves were obtained for all the gap and test speed conditions, and representative axial fracture strains were obtained. The measured fracture strain from different gaps and test speeds are given in Table 3 with the associated standard errors.

In general, an increasing trend in fracture strain was observed with increasing test speed which is due to the change in flow stress, dynamic recovery or adiabatic heating effect at higher strain rates, different slip systems and differences in dislocation mobility [71, 72]. Similar to this observation, Smerd, et al. [5] reported a small increase in the elongation at fracture when AA5182 parent aluminium alloy sheet was tested at different strain rates. These fracture strains are important criteria to use in the constitutive model for evaluating the joint behaviour during crash simulations.

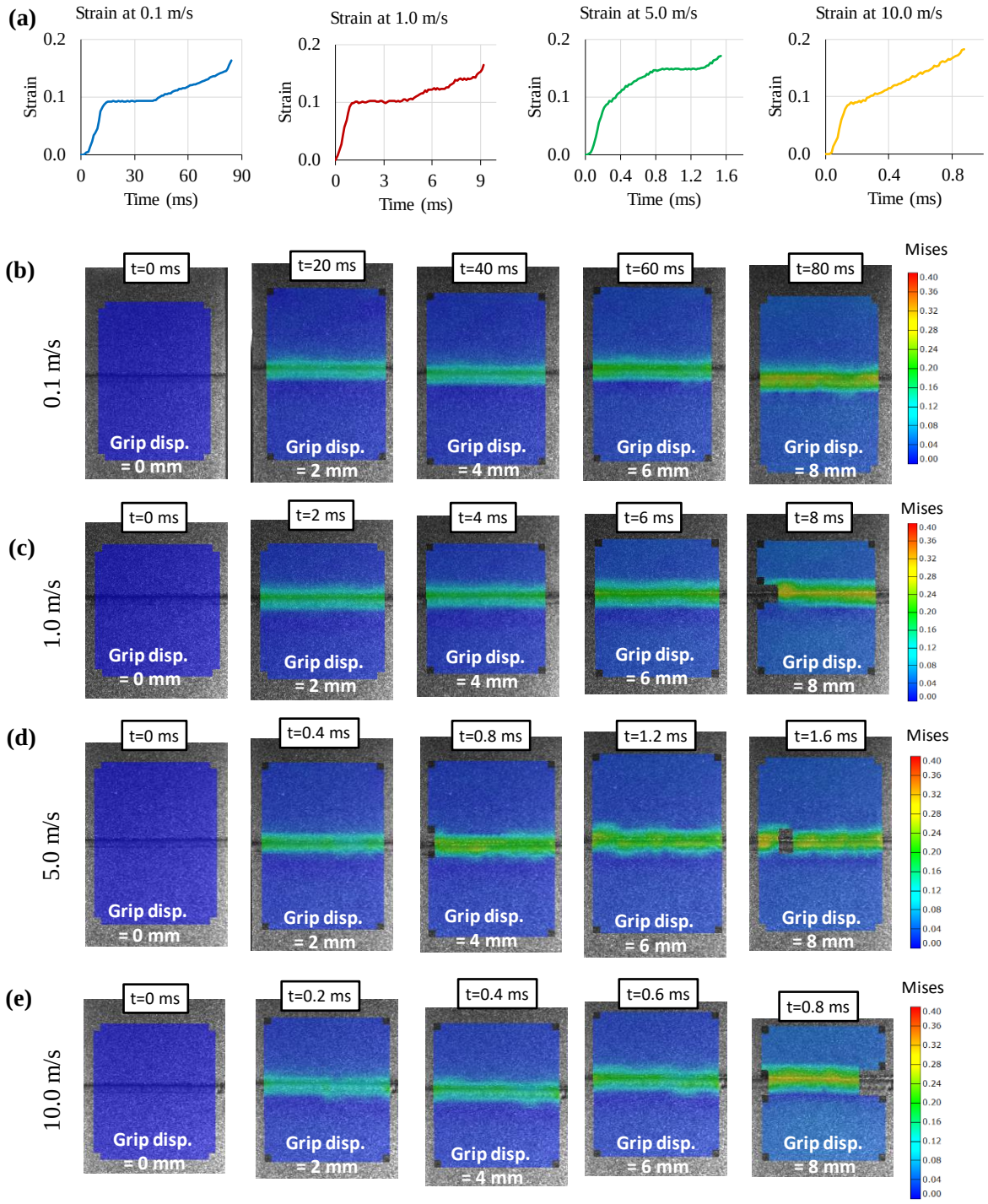

Figure 8 DIC based axial strain measurement at different tensile rates for 0.2 mm gap-bridged fillet edge weld (a) axial strain development curves across weld area at different rates using a local gauge length of 4.08 mm across the weld, (b) sequences of the high-speed digital images and associated strain maps obtained from 0.1 m/s test, (c) sequences of the high-speed digital images and associated strain maps obtained from 1.0 m/s test, (d) sequences of the high-speed digital images and associated strain maps obtained from 5.0 m/s test, and (d) sequences of the high-speed digital images and associated strain maps obtained from 10.0 m/s test.

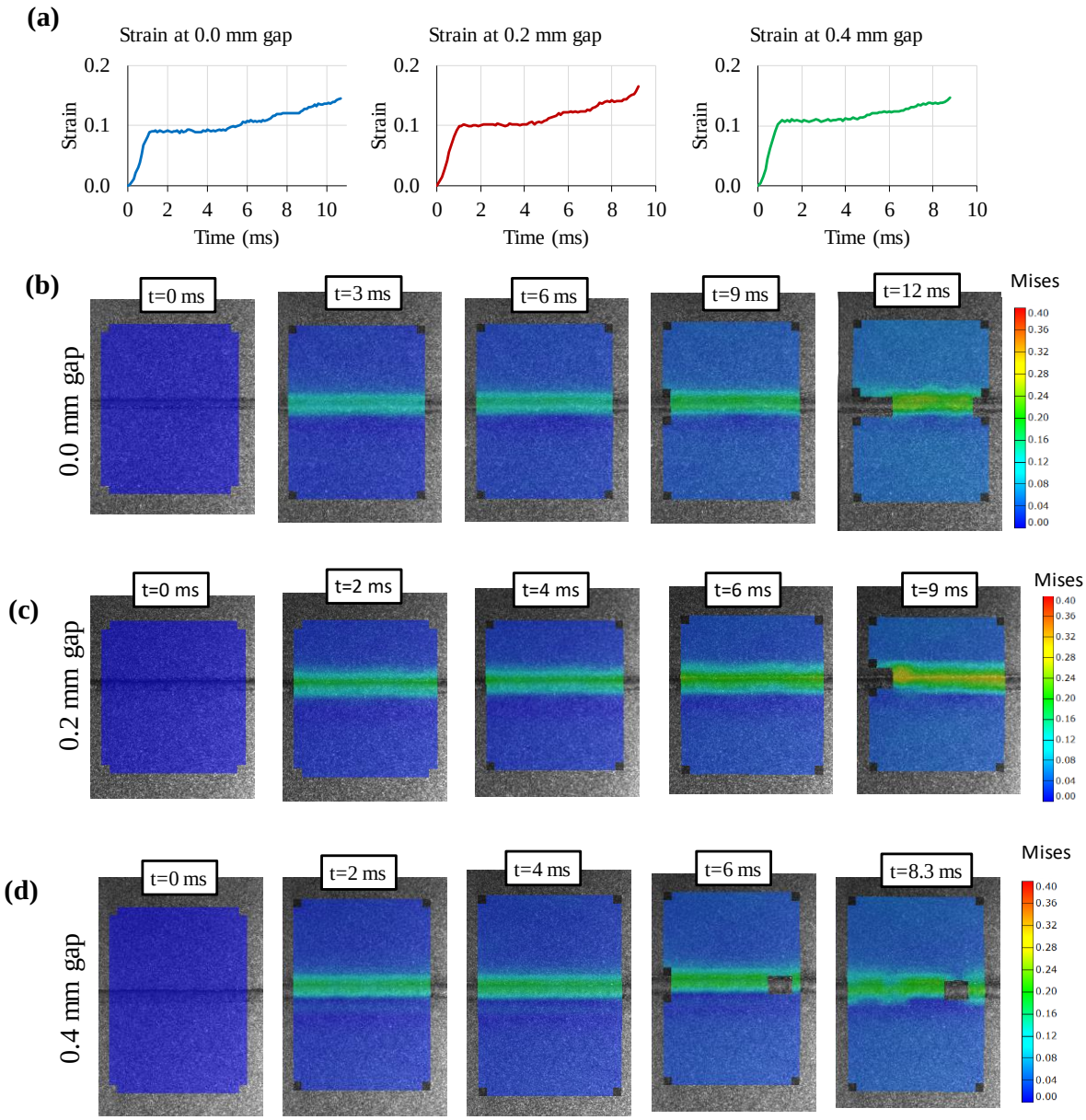

Figure 9 DIC based axial strain measurement (a) strain development curves for different gaps at a rate of 1.0 m/s using a local gauge length of 4.08 mm across the weld, (b) zero gap based fillet edge weld strain distribution from the start of the test to near fracture, (c) 0.2 mm gap bridged fillet edge weld train distribution from the start of the test to near fracture, and (d) 0.4 mm gap bridged fillet edge weld train distribution from the start of the test to near fracture.

Table 3 Average fracture obtained from different part-to-part gaps and test speeds.

Fracture strain at failure					
		Test speed			
		0.1 m/s	1.0 m/s	5.0 m/s	10.0 m/s
Part-to-part gap	0.0 mm	0.141 ± 0.007	0.159 ± 0.003	0.169 ± 0.005	0.180 ± 0.008
	0.2 mm	0.153 ± .007	0.166 ± 0.008	0.186 ± 0.002	0.181 ± 0.005
	0.4 mm	0.140 ± 0.005	0.147 ± 0.004	0.172 ± 0.002	0.194 ± 0.002

3.3. Joint finite element modelling

Finite element analysis (FEA) is widely utilised as a modelling tool to replicate the results obtained from the physical test or to predict actual response during complex scenarios, such as crash events. To simulate the load-displacement curves of gap-bridged laser weld, finite element models were developed for different gap conditions in LS-DYNA. In general, automotive body-in-white crash simulation is based on shell elements due to computational efficiency [79]. Papadakis, et al. [80] stressed the importance of including forming, trimming and welding models within automotive structures to predict the structural behaviour at early stages of product and process planning. For model tractability and easy integration with automotive body-in-white assembly, the base material was modelled using shell elements which is common practice for modelling sheet metal parts. However, solid elements give more accurate results in comparison with shell elements as they are more suitable to calculate stress in all the three directions. Therefore, a solid cubic mesh was chosen to represent the weld zone which also can easily represent the part-to-part gaps. The finite element model of the test specimen with subsections and other elements included in the model are shown in Figure 10. The models were composed of fusion zone (i.e. weld), upper part, lower part, static grip and moving grip and elastic spring.

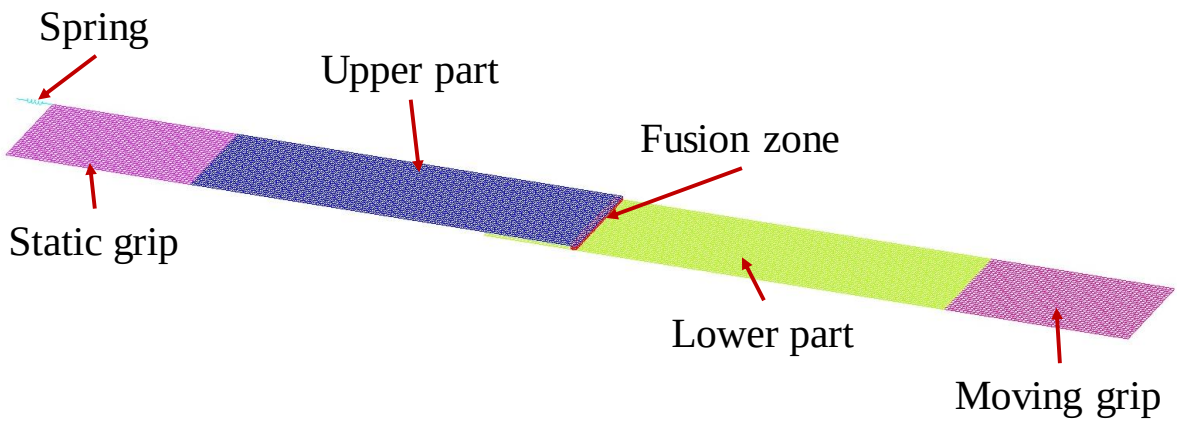

Figure 10 Schematic of finite element mesh model set-up of lap shear test specimen.

The upper part, lower part, static grip and moving grip were modelled using fully integrated shell elements with standard Belytschko-Tsay membrane formulation. An initial mesh sensitivity analysis was performed for the shell elements by changing the mesh size and a rectangular element of dimensions 0.5 mm × 0.5 mm was selected for this study as mesh sensitivity was low for this size of element. In contrast, the weld fusion zone was modelled using a solid brick mesh with fully integrated quadratic 8 node element with nodal rotations. Mesh sensitivity was again performed to model the fusion zone. A single layer of solid elements was not sufficient to replicate the experimental behaviour and early fracture was observed with excessive distortion. In this study, a 3×3 layer of solid elements was used and extruded in the welding direction as a further increase in the number of elements had no significant improvement. Therefore, element size was varying from 0.3 to 0.5 mm and they were sufficient to replicate the fusion zone behaviour. Additionally, by increasing the element size of the solid elements, part-to-part gaps were easily modelled. An elastic spring to replicate the load cell was added to the static grip for capturing the load during the lap shear tests. Appropriate selection of the elastic spring stiffness value is essential to avoid noise in the initial loading response. When a high value of spring stiffness was chosen, an initial ripple was observed within the load-displacement curve. Thereafter, stiffness was slowly reduced to eliminate the ripple and it was observed that an elastic spring stiffness of 100,000 N/m was required to remove the unwanted noise from the measured load. Additionally, a smooth load sequence (i.e. a small acceleration time to reach the required velocity and then constant velocity for the rest of the test) was applied to remove the initial loading noise. The static and moving grips were modelled as rigid bodies where the static grip was constrained with all 6 DOFs and the moving grip was displaced in the loading direction with a velocity profile. Fully integrated elements were selected to remove the hourglass effect when the MAT_024: Piecewise Linear Plasticity material model [81] was used to model the material properties of the base material

as well as weld fusion zone. Additionally, two contacts were introduced in between (i) the upper part and the weld, and (ii) the lower part and the weld when the weld zone was assigned to the slave side and the larger base material parts (i.e. upper and lower parts) were assigned to master side to achieve consistency in the model. By utilising contact-based modelling, the weld fusion zone can be placed easily without modifying the geometry or mesh which made this model adaptable for integration with body-in-white simulation. Additionally, the fusion zone scale factor and localised fracture strain are equally important to simulate the identical failure location and failure mode obtained from test data. The fusion zone scale factor was used to define the stress-strain behaviour of the fusion zone by modifying the stress-strain curve of the base material. The value of the fusion zone scale factor was derived from the microhardness changes in the fusion zone. In general, it was observed that the average microhardness increased in the weld zone when AA5182 material was used [16, 18]. A detailed microhardness study was reported by Das, et al. [18] with microhardness changes from base material to fusion zone. They reported around 10% increase of microhardness values in the fusion zone compared to the base material due to uniform diffusion of Mg particles and grain characteristics. Readers interested in relationship between detailed microstructural and mechanical/metallurgical properties including microhardness profiles are redirected to Das, et al. [18]. The stress – strain curve for the material in the fusion zone was therefore taken as that for the base material increased by a factor of 1.1 which was the fusion zone scale factor. The localised fracture strain was also important to obtain the fracture at required grip displacement. This fracture strain was selected to terminate the simulations when the experimentally measured displacement-to-failure was reached. The base material data used in this simulation was given in Table 1. Additionally, the other specific details are listed in Table 4. The stress-strain behaviour of the base material was incorporated into the material model using a tabulated approach available in LS-DYNA. As the rate sensitivity was admittedly low, the same model could be used to

describe the load-displacement behaviour at different test speeds with only a minor increase in localised fracture strain value.

As the load-displacement behaviours are quite similar for the applied tensile rates, 1.0 m/s was selected as test speed to develop a finite element model for varying gap-bridged fillet edge welds. The load-displacement curves obtained from the simulation and average test data obtained from experiments are plotted for 0.0 mm, 0.2 mm and 0.4 mm gap-bridged fillet edge welds in Figure 11(a). For ease of understanding, the fracture points are cross marked for the experimental tests and corresponding simulation. Figure 11(b) shows the sequence of the simulation stages and associated strain maps obtained from zero gap fillet edge weld at 1.0 m/s test. Six strain maps are plotted to represent (1) start of the loading cycle, (2) at the end of elastic increment, (3) at the end of the plastic plateau, (4) near the middle of plastic increment, (5) before fracture, and (6) after the fracture.

Table 4 Additional material data and parameters used to develop the FE model.

Properties	Description/Value
Element type	Discrete – for spring-based load cell Shell – for upper part, lower part, static grip and moving grip Solid – for fusion zone (i.e. weld)
Elastic spring stiffness (N/m)	100000.0
Rigid body constraints	Constraints in Y and Z displacement (as X corresponds to grip displacement), Constraints in X, Y and Z rotation
Fusion zone scale factor	1.1
Localised fracture strain	Varied based on fracture point in experimental load-displacement curve
Contact between BM and weld	TIED_SURFACE_TO_SURFACE (as defined in LS-DYNA)

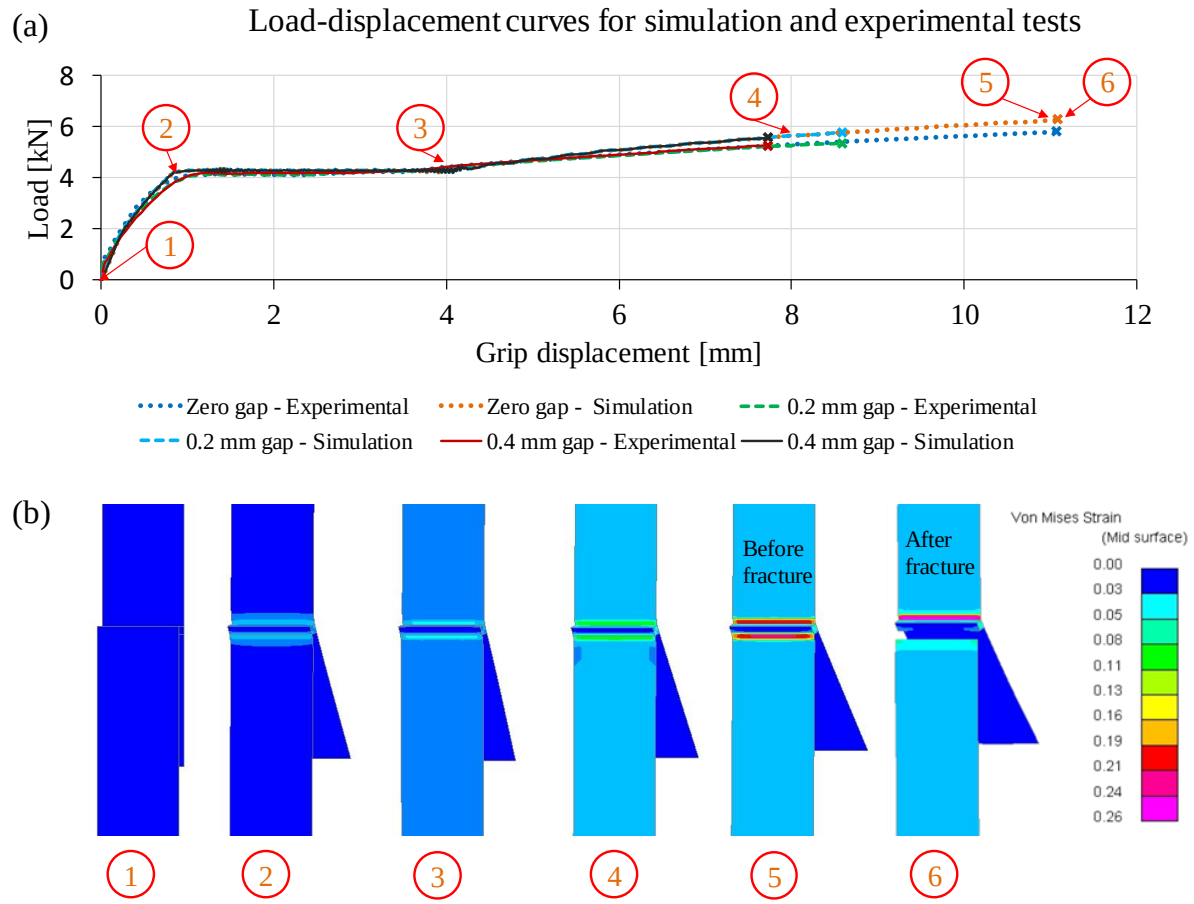

Figure 11 (a) Load-displacement curves from simulation and experimental tests for zero gap, 0.2 mm and 0.4 mm gap-bridged fillet edge welds, and (b) image stages obtained from simulation to show strain distribution when zero gap fillet edge weld simulated at a rate of 1.0 m/s test.

This model is useful for integration with body-in-white assembly simulations requiring laser joints to be modelled and different part-to-part gap conditions can be easily simulated by varying the fracture strain. For example, the fracture strain was 0.51 for the zero gap based weld but must be reduced to 0.30 and 0.289 to obtain the fracture points matching with the test data for 0.2 mm and 0.4 mm gap-bridged fillet edge welds respectively. Therefore, by altering the fracture strain, different gap bridged welds can be represented which make this model adaptable for crash simulation.

As there is no significant change in yield strength in between -50°C to 100°C and gap-bridged fillet edge welds exhibit the same load-displacement behaviour, the aforementioned MAT_024: Piecewise Linear Plasticity material model was used to simulate them and different fracture points were obtained by varying the fracture strain values. However, the load-displacement characteristics were not the same at 200°C and 300°C. To model the effects of these elevated temperatures on the RLW fillet edge welds, the tabulated Johnson-Cook (J-C) model was adapted in this study where the effects of temperature on the flow stress can be represented as tabulated curves. Similar to the original J-C material model, the flow stress (σ_y) is expressed as a function of plastic strain (ε), plastic strain rate ($\dot{\varepsilon}$), and temperature (T) via the following formula

$$\sigma_y = k_1(\varepsilon, \dot{\varepsilon}) \frac{k_t(\varepsilon, T)}{k_t(\varepsilon, T_R)} \quad (1)$$

where, $k_1$and k_t are the load curves or tables correspond to plastic strain response and temperature-dependent plastic strain response respectively. Furthermore, T_R represents the material properties at room temperature. With the general tabulated input parameters, the temperature-dependent behaviour was simulated.

As the flow curves were changed at 200°C and 300°C, the room temperature flow curve was reverse engineered to simulate the load-displacement characteristics and validated with RLW fillet edge weld. The load-displacement characteristics for zero gap fillet edge weld at 200°C and 300°C are shown in Figure 12(a). It can be seen that load at the plastic region is reduced considerably when the test temperature was increased from 200°C to 300°C. For example, at a grip displacement of 10 mm, there was a load drop of 0.74 kN when the temperature was increased from 200°C to 300°C. The failure modes obtained from the simulation at 200°C and 300°C are similar to the failure modes obtained from actual tests as shown in Figure 12(b).

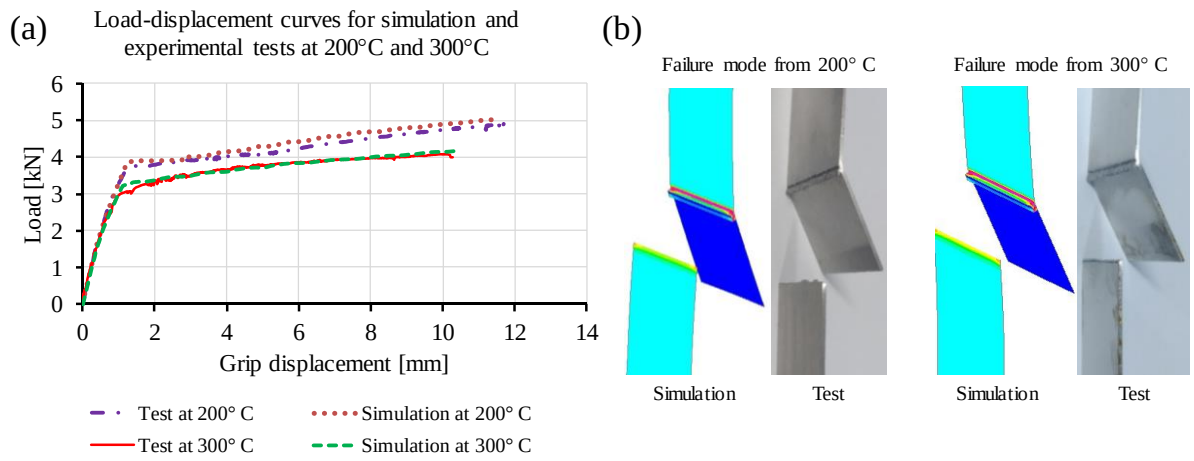

Figure 12 (a) Load-displacement curves from simulation and experimental tests for zero gap fillet edge welds at 200°C and 300°C, and (b) failure modes at 200°C and 300°C.

3.4. Comparative study with other joining methods

Two industrially used joining methods for automotive body-in-white applications are self-piercing riveting (SPR) and resistance spot welding (RSW). For the comparative study, SPR and RSW lap joints were made by carefully placing the rivet or weld nugget at the centre of the overlap region as shown in Figure 13. Guidelines are available to join a range of materials using SPR to obtain the required quality for industrial application [82, 83]. Furthermore, Pickin, et al. [84] and Li, et al. [82] have described the various detailed aspects of self-piercing riveting including important process parameters, rivet selection, profile of die to be used and suitable materials for SPR joining. The SPR joints were produced using a nominal 5 mm shank diameter hardened steel rivets from the Tucker® SPR system. The rivet and up setting die combinations (i.e. rivet C5.3 ×5H0, die M260 416) were used for joining two sheets of AA5182 of 1.0 mm thickness, in this study, as recommended by the manufacturer. Head height is one of the most critical parameters for the SPR joint strength which can be measured and is the difference between the rivet head and the top sheet surface after producing the joint. In this study, a head height of -0.80 mm was chosen based on the recommendation of the manufacturers as well as relying on the pilot experimentation results. The resistance spot welded test specimens were

prepared using a DENGENSHA 100 KVA MFDC Pedestal Spot Welding Machine having rated capacity of 100 KVA at 50% duty cycle and maximum electrode force of 10 kN. The electrode material used was Z-TRODE® which is an alloy of zirconium and oxygen-free copper. The main RSW welding process parameters reported in the literature are weld current, welding time, sheet thickness, material type, geometry of electrodes and electrode force [85, 86]. The process parameters used to produce RSW joints in this study are listed in Table 5 and were obtained after initial screening trials and recommendations from automotive manufacturers.

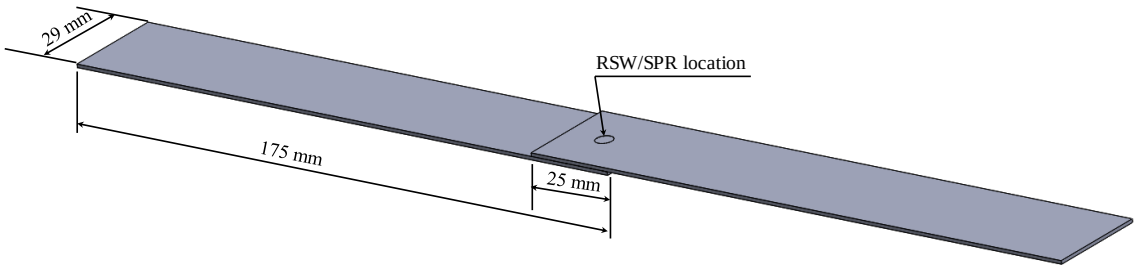

Figure 13 SPR and RSW lap configuration samples with rivet or weld nugget at the centre of the overlap region.

Table 5 Process parameters used to produce RSW joints.

Process parameters	Main Weld Current (KA)	Squeeze Time (ms)	Weld Time (ms)	Hold Time (ms)	Electrode Force (kN)	RSW Electrode Tip Face Diameter (mm)
Value	26.0	500	80	300	4.70	M20/R100

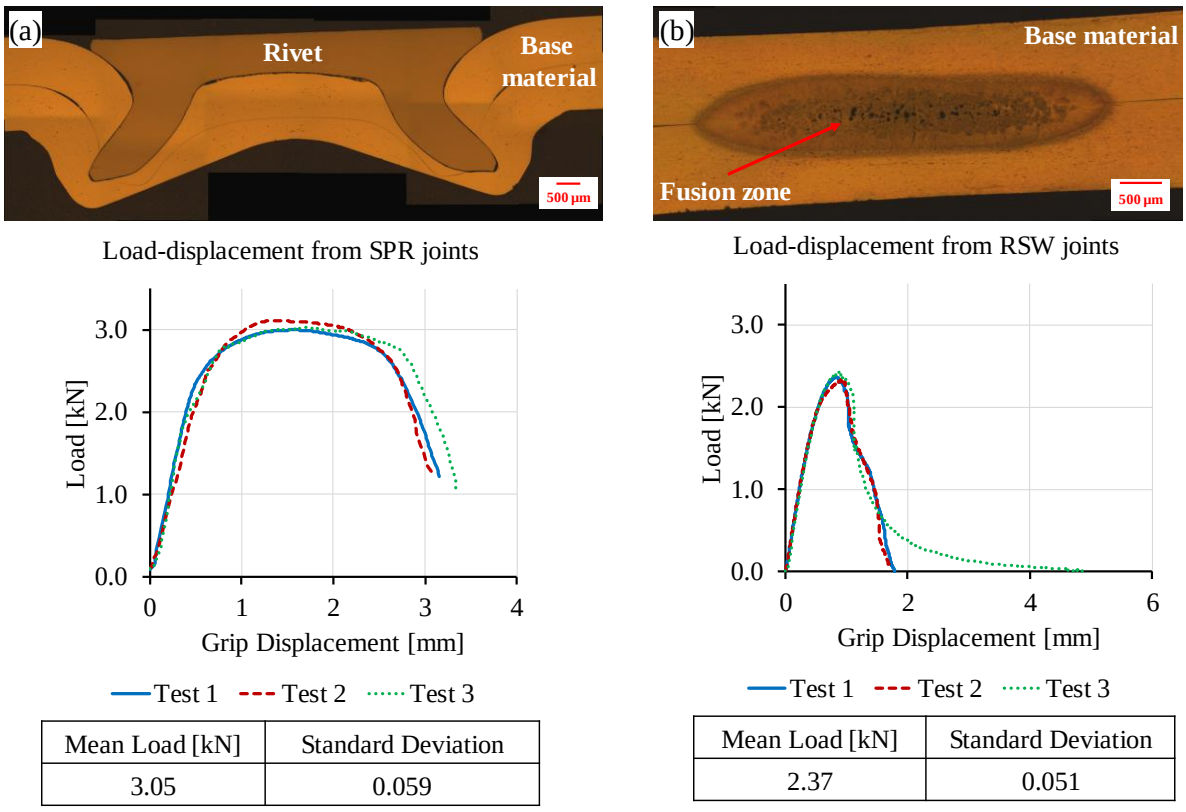

Mean Load [kN]	Standard Deviation
3.05	0.059

Mean Load [kN]	Standard Deviation
2.37	0.051

Figure 14 The cross-sectional images and load-displacement curves from lap shear tests at 0.1 m/s from (a) self-piercing revering (SPR), and (b) resistance spot welding (RSW).

Similar to RLW gap-bridged joint testing, three repeats were conducted on the SPR and RSW samples. Wood, et al. [64] conducted a detailed study on high rate performance of self-piercing riveted joints in aluminium sheet (A5754) and they concluded that the strain rate sensitivity of SPR joints was low. A similar observation was made by Sun and Khaleel [77] where they reported that the strength increase from moderate (4.47 m/s or 10 mph) to high speed (8.94 m/s or 20 mph) was not as significant when they tested self-piercing rivets (SPR) and resistance spot welds (RSWs). As low strain rate sensitivity was observed and also reported in the literature, a test speed of 0.1 m/s was chosen for this comparative study which also minimised the noise within the test data. The cross-sectional images accompanied with load-displacement characteristics of SPR and RSW joints are shown in Figure 14 with mean loads and standard deviations obtained from the corresponding tests. Unlike the one-sided RLW process, both the

SPR and RSW processes need two-sided access to apply additional force to close the part-to-part gap, if any. This part-to-part intimate contact is necessary for the formation of joints by both SPR and RSW processes. As a result, only zero gap based joints can be achieved for SPR and RSW whereas being a non-contact process, the part-to-part gap is needed to be bridged by RLW. Therefore, the mean loads obtained from the different part-to-part gap-bridged RLW joints were compared with SPR and RSW joints. Figure 15 (a) shows the mean load from 29 mm long RLW seam weld at different gap conditions against 5 mm diameter SPR joints and approximately 5 mm nugget diameter RSW joints. It can be observed that 29 mm RLW stitches exhibit higher strength (i.e. 5.54 kN at zero gap, 5.02 kN at 0.2 mm gap and 4.751 at 0.4 mm gap) than the SPR (i.e. 3.05 kN) and RSW (i.e. 2.37 kN) joints. Under this condition, it can be concluded that one SPR or RSW joint strength is equivalent to 16 mm or 12.5 mm RLW seam at zero part-to-part gap condition, respectively. From Figure 15(a), it can be noted that the minimum RLW joint strength was obtained from the 0.4 mm part-to-part gap-bridged fillet edge weld. Therefore, the 0.4 mm gap-bridged RLW joint tested at 0.1 m/s was selected for comparison with RSW and SPR joints to understand the differences in energy absorption as shown by the load-displacement curves in Figure 15(b). It can be noted that the area (equivalent to energy absorption) under the 0.4 mm gap-bridged RLW curve is 3 and 9 times higher than the SPR and RSW curves, respectively.

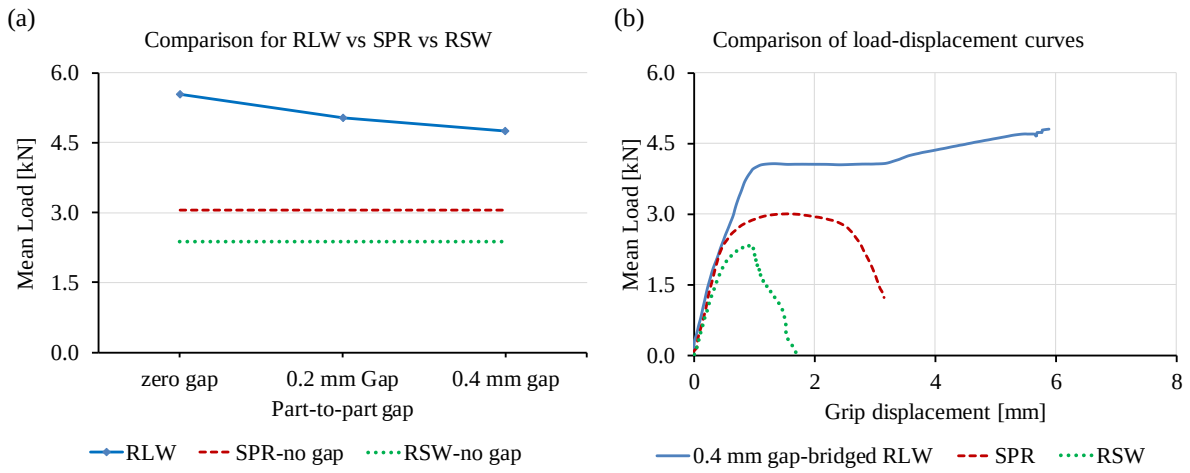

Figure 15 Comparison of (a) mean loads from RLW (29 mm long stitches), SPR (single rivet of 5 mm diameter) and RSW (single nugget of 5 mm diameter approx.), and (b) load-displacement curves from 0.4 mm gap-bridged RLW, SPR and RSW joints.

4. Conclusions

High rate tensile characterisation was reported considering the fillet edge joints produced by *'gap-bridged'* remote laser welding (RLW) using the common automotive-grade AA5182 aluminium alloy. Three gap-bridged conditions (i.e. no gap, 0.2 mm and 0.4 mm part-to-part gaps) were investigated to evaluate rate sensitivity over the test speed ranges from moderate (0.1 m/s) to high speed (10 m/s). Furthermore, the gap-bridged RLW joints are compared with two other industrial standard joining methods. This study has demonstrated the following:

- In general, the strain rate sensitivity of RLW gap-bridged fillet edge welds was low. Small increments in load were observed with the increasing rate of test speed together with an increase in grip displacement at failure.
- Both the average mean load and average grip displacement at failure decreased with increasing part-to-part gap values. Therefore, no or low part-to-part gaps are preferred for industrial application.

- This paper reported the loss of joint strength beyond 200°C due to reduction in flow stress and yield strength. Similarly, a gradual decrease in grip displacement at failure was obtained with increasing temperature.
- Strain localisation was obtained within the elastic region due to asymmetric deformation behaviour and fracture strain increased with increasing test speed.
- An efficient macro scale simulation model was developed to capture the accurate behaviour of the RLW weld for model tractability and could be used for easy integration with automotive body-in-white assembly.
- Furthermore, by incorporating the depressed and elevated temperatures into the FE model, material and process designers can be benefitted while designing the joints, i.e. length of joint or location of joints to achieve the desired structural strength.
- Gap-bridged RLW was compared with SPR and RSW for automotive body-in-white applications. It demonstrated the suitability of RLW joint especially when energy absorption was considered.

In conclusion, RLW has been shown to be an effective method for joining aluminium alloy structures where fit-up gaps need to be tolerated and the resulting joints can perform as well or better than the more commonly used RSW or SPR joints in terms of energy absorption. The gap-bridged RLW joints can also be represented by a macroscale simulation which can accommodate deformation both high-speed (crash) and at the extremes of the service temperature range. This could provide crash/design engineers a valuable tool to evaluate joint integrity under crash conditions at early stage of the design process.

Acknowledgements

This research is partially supported by Scansonic IPT GmbH with laser experimental trials. Characterisation and testing were provided by the WMG Centre High Value Manufacturing (HVM) Catapult at The University of Warwick.

Reference

[1] E. Commission, Amending Regulation (EC) No 443/2009 to define the modalities for reaching the 2020 target to reduce CO2 emissions from new passenger cars, Official Journal of the European Union (2014).

[2] U. government, Climate Change Act, Received Royal Assent 26 (2008).

[3] A. Das, D. Li, D. Williams, D. Greenwood, Joining Technologies for Automotive Battery Systems Manufacturing, World Electric Vehicle Journal 9(2) (2018) 22.

[4] W.S. Miller, L. Zhuang, J. Bottema, A.J. Wittebrood, P. De Smet, A. Haszler, A. Vieregge, Recent development in aluminium alloys for the automotive industry, Materials Science and Engineering: A 280(1) (2000) 37-49.

[5] R. Smerd, S. Winkler, C. Salisbury, M. Worswick, D. Lloyd, M. Finn, High strain rate tensile testing of automotive aluminum alloy sheet, International Journal of Impact Engineering 32(1) (2005) 541-560.

[6] M. Kirchhoff, Laser applications in battery production — From cutting foils to welding the case, 2013 3rd International Electric Drives Production Conference (EDPC), 2013, pp. 1-3.

[7] A. Das, A. Barai, I. Masters, D. Williams, Comparison of tab-to-busbar ultrasonic joints for electric vehicle Li-ion battery applications, World Electric Vehicle Journal 10(3) (2019) 55.

[8] S. Dhara, A. Das, Impact of ultrasonic welding on multi-layered Al–Cu joint for electric vehicle battery applications: A layer-wise microstructural analysis, Materials Science and Engineering: A 791 (2020) 139795.

[9] J. Hirsch, Recent development in aluminium for automotive applications, Transactions of Nonferrous Metals Society of China 24(7) (2014) 1995-2002.

[10] L. Quintino, R. Miranda, U. Dilthey, D. Iordachescu, M. Banasik, S. Stano, Laser Welding of Structural Aluminium, in: P.M.G.P. Moreira, L.F.M. da Silva, P.M.S.T. de Castro (Eds.), Structural Connections for Lightweight Metallic Structures, Springer Berlin Heidelberg, Berlin, Heidelberg, 2012, pp. 33-57.

[11] A. El-Batahgy, M. Kutsuna, Laser beam welding of AA5052, AA5083, and AA6061 aluminum alloys, Advances in Materials Science and Engineering (2009).

[12] A. Ambroziak, M. Korzeniowski, Using Resistance Spot Welding for Joining Aluminium Elements in Automotive Industry, Archives of Civil and Mechanical Engineering 10(1) (2010) 5-13.

[13] L. Deng, Y. Li, B.E. Carlson, D.R. Sigler, Effects of electrode surface topography on aluminum resistance spot welding, Welding Journal 97(4) (2018) 120s-132s.

[14] X. He, I. Pearson, K. Young, Self-pierce riveting for sheet materials: state of the art, Journal of Materials Processing Technology 199(1-3) (2008) 27-36.

[15] P. Briskham, N. Blundell, L. Han, R. Hewitt, K. Young, D. Boomer, Comparison of self-pierce riveting, resistance spot welding and spot friction joining for aluminium automotive sheet, SAE Technical Paper, 2006.

[16] C. Leitao, R.M. Leal, D.M. Rodrigues, A. Loureiro, P. Vilaça, Mechanical behaviour of similar and dissimilar AA5182-H111 and AA6016-T4 thin friction stir welds, Materials & Design 30(1) (2009) 101-108.

[17] H. Uzun, C. Dalle Donne, A. Argagnotto, T. Ghidini, C. Gambaro, Friction stir welding of dissimilar Al 6013-T4 To X5CrNi18-10 stainless steel, Materials & Design 26(1) (2005) 41-46.

[18] A. Das, I. Butterworth, I. Masters, D. Williams, Microstructure and mechanical properties of gap-bridged remote laser welded (RLW) automotive grade AA 5182 joints, Materials Characterization 145 (2018) 697-712.

[19] M. Pakdil, G. Çam, M. Koçak, S. Erim, Microstructural and mechanical characterization of laser beam welded AA6056 Al-alloy, Materials Science and Engineering: A 528(24) (2011) 7350-7356.

[20] A.K. Dasgupta, J. Mazumder, Laser welding of zinc coated steel: an alternative to resistance spot welding, Science and Technology of Welding and Joining 13(3) (2008) 289-293.

[21] A. Das, P. Franciosa, D. Ceglarek, Fixture design optimisation considering production batch of compliant non-ideal sheet metal parts, Procedia Manufacturing 1 (2015) 157-168.

[22] A. Das, Shape variation modelling, analysis and statistical control for assembly system with compliant parts, WMG, University of Warwick, 2016.

741 [23] S. Sun, D. E, The investigation of time-dependent springback for AC170PX aluminum alloy at
742 room temperature, Materials & Design 93 (2016) 118-127.
743 [24] A. Das, P. Franciosa, D. Williams, D. Ceglarek, Physics-driven shape variation modelling at early
744 design stage, Procedia CIRP 41 (2016) 1072-1077.
745 [25] M. Allen, M. Oliveira, S. Hazra, O. Adetoro, A. Das, R. Cardoso, Benchmark 2 – Springback of a
746 Jaguar Land Rover Aluminium, Journal of Physics: Conference Series 734(2) (2016) 022002.
747 [26] A. Das, P. Franciosa, S. Gerbino, D. Williams, Prediction of Geometric Errors of Stamped Sheet
748 Metal Parts using Deviation Field Decomposition, International Conference on Competitive
749 Manufacturing (COMA), Stellenbosch, South Africa, 2016, pp. 109-114.
750 [27] A. Das, P. Franciosa, A. Pesce, S. Gerbino, Parametric Effect Analysis of Free-form Shape Error
751 during Sheet Metal Forming, International Journal of Engineering Science and Technology 9(09S)
752 (2017) 117-124.
753 [28] B. Li, B.W. Shiu, K.J. Lau, Robust fixture configuration design for sheet metal assembly with laser
754 welding, Journal of Manufacturing Science and Engineering 125(1) (2003) 120-127.
755 [29] B. Li, B.W. Shiu, Principle and simulation of fixture configuration design for sheet metal assembly
756 with laser welding, part 2: optimal configuration design with genetic algorithm, Int J Adv Manuf
757 Technol 18(4) (2001) 276-284.
758 [30] B. Li, B.W. Shiu, K.J. Lau, Principle and simulation of fixture configuration design for sheet metal
759 assembly with laser welding, part 1: finite-element modelling and a prediction and correction method,
760 Int J Adv Manuf Technol 18(4) (2001) 266-275.
761 [31] B. Schleich, N. Anwer, L. Mathieu, S. Wartzack, Skin model shapes: A new paradigm shift for
762 geometric variations modelling in mechanical engineering, Computer-Aided Design 50 (2014) 1-15.
763 [32] A. Das, P. Franciosa, P.K.S. Prakash, D. Ceglarek, Transfer function of assembly process with
764 compliant non-ideal parts, Procedia CIRP 21(0) (2014) 177-182.
765 [33] F. Albert, P. Marben, T. Graham, Remote Laser Welding of Steel and Aluminum Alloys, Laser
766 Technik Journal 14(1) (2017) 32-35.
767 [34] P. Fixemer, F. Albert, P. Sievi, T. Graham, Seam Guided Laser Remote Welding with Automated
768 Gap Bridging, Laser Technik Journal 12(2) (2015) 38-41.
769 [35] A. Müller, S.-F. Goecke, P. Sievi, F. Albert, M. Rethmeier, Laser Beam Oscillation Strategies for
770 Fillet Welds in Lap Joints, Physics Procedia 56 (2014) 458-466.
771 [36] A. Das, I. Butterworth, I. Masters, D. Williams, Evaluation of Key Geometrical and Mechanical
772 Properties for Remote Laser Welded AC-170PX Aluminium Joints, Journal of Laser
773 Micro/Nanoengineering 14(1) (2019) 1-7.
774 [37] L. Djapic Oosterkamp, A. Ivankovic, G. Venizelos, High strain rate properties of selected
775 aluminium alloys, Materials Science and Engineering: A 278(1) (2000) 225-235.
776 [38] A. Rusinek, J.A. Rodríguez-Martínez, Thermo-viscoplastic constitutive relation for aluminium
777 alloys, modeling of negative strain rate sensitivity and viscous drag effects, Materials & Design 30(10)
778 (2009) 4377-4390.
779 [39] Y.C. Lin, Y.-C. Xia, X.-M. Chen, M.-S. Chen, Constitutive descriptions for hot compressed 2124-
780 T851 aluminum alloy over a wide range of temperature and strain rate, Computational Materials
781 Science 50(1) (2010) 227-233.
782 [40] S.A. Hosseini Kordkheili, M.M. Ashrafian, H. Toozandehjani, A rate-dependent constitutive
783 equation for 5052 aluminum diaphragms, Materials & Design 60 (2014) 13-20.
784 [41] T. Rahmaan, A. Bardelcik, J. Imbert, C. Butcher, M.J. Worswick, Effect of strain rate on flow
785 stress and anisotropy of DP600, TRIP780, and AA5182-O sheet metal alloys, International Journal of
786 Impact Engineering 88 (2016) 72-90.
787 [42] A. Jenab, I. Sari Sarraf, D.E. Green, T. Rahmaan, M.J. Worswick, The Use of genetic algorithm
788 and neural network to predict rate-dependent tensile flow behaviour of AA5182-O sheets, Materials &
789 Design 94 (2016) 262-273.
790 [43] A. Pandey, A.S. Khan, E.-Y. Kim, S.-H. Choi, T. Gnäupel-Herold, Experimental and numerical
791 investigations of yield surface, texture, and deformation mechanisms in AA5754 over low to high
792 temperatures and strain rates, International Journal of Plasticity 41 (2013) 165-188.
793 [44] L. Chen, G. Zhao, J. Yu, Hot deformation behavior and constitutive modeling of homogenized
794 6026 aluminum alloy, Materials & Design 74 (2015) 25-35.

[45] D. Trimble, G.E. O'Donnell, Constitutive Modelling for elevated temperature flow behaviour of AA7075, Materials & Design 76 (2015) 150-168.
[46] K. Zheng, D.J. Politis, L. Wang, J. Lin, A review on forming techniques for manufacturing lightweight complex—shaped aluminium panel components, International Journal of Lightweight Materials and Manufacture 1(2) (2018) 55-80.
[47] T. Mukai, K. Higashi, S. Tanimura, Influence of the magnesium concentration on the relationship between fracture mechanism and strain rate in high purity Al-Mg alloys, Materials Science and Engineering: A 176(1) (1994) 181-189.
[48] K. Higashi, T. Mukai, K. Kaizu, S. Tsuchida, S.J.L.J.d.P.I. Tanimura, Strain rate dependence on mechanical properties in some commercial aluminum alloys, 1(C3) (1991) C3-341-C3-346.
[49] T.R.B. Grandjean, J. Groenewald, J. Marco, The experimental evaluation of lithium ion batteries after flash cryogenic freezing, Journal of Energy Storage 21 (2019) 202-215.
[50] D. Ouyang, M. Chen, Q. Huang, J. Weng, Z. Wang, J. Wang, A review on the thermal hazards of the lithium-ion battery and the corresponding countermeasures, Applied Sciences 9(12) (2019) 2483.
[51] P.T. Summers, Y. Chen, C.M. Rippe, B. Allen, A.P. Mouritz, S.W. Case, B.Y. Lattimer, Overview of aluminum alloy mechanical properties during and after fires, Fire Science Reviews 4(1) (2015) 3.
[52] R. Bobbili, V. Madhu, A.K. Gogia, Tensile behaviour of aluminium 7017 alloy at various temperatures and strain rates, Journal of Materials Research and Technology 5(2) (2016) 190-197.
[53] H. Hamasaki, Y. Morimitsu, F. Yoshida, Stress relaxation of AA5182-O aluminum alloy sheet at warm temperature, Procedia Engineering 207 (2017) 2405-2410.
[54] N. Farabi, D.L. Chen, J. Li, Y. Zhou, S.J. Dong, Microstructure and mechanical properties of laser welded DP600 steel joints, Materials Science and Engineering: A 527(4) (2010) 1215-1222.
[55] Y. Liu, D. Dong, L. Wang, X. Chu, P. Wang, M. Jin, Strain rate dependent deformation and failure behavior of laser welded DP780 steel joint under dynamic tensile loading, Materials Science and Engineering: A 627 (2015) 296-305.
[56] D. Dong, Y. Liu, Y. Yang, J. Li, M. Ma, T. Jiang, Microstructure and dynamic tensile behavior of DP600 dual phase steel joint by laser welding, Materials Science and Engineering: A 594 (2014) 17-25.
[57] Q. Jia, W. Guo, P. Peng, M. Li, Y. Zhu, G. Zou, Microstructure- and Strain Rate-Dependent Tensile Behavior of Fiber Laser-Welded DP980 Steel Joint, Journal of Materials Engineering and Performance 25(2) (2016) 668-676.
[58] B.E.I. 26203-2, Metallic materials. Tensile testing at high strain rates. Servo-hydraulic and other test systems, BSI Standards Publication, 2011.
[59] P.K.C. Wood, C.A. Schley, R.T. Limited, Strain Rate Testing of Metallic Materials and Their Modeling for Use in CAE Based Automotive Crash Simulation Tools, iSmithers2009.
[60] J. Li, J.E. Carsley, T.B. Stoughton, L.G. Hector, S.J. Hu, Forming limit analysis for two-stage forming of 5182-O aluminum sheet with intermediate annealing, International Journal of Plasticity 45 (2013) 21-43.
[61] M. Bhargava, A. Tewari, S. Mishra, Strain path diagram simulation of AA 5182 Aluminum alloy, Procedia Engineering 64 (2013) 1252-1258.
[62] D. Colombo, B. Previtali, Laser dimpling and remote welding of zinc-coated steels for automotive applications, Int J Adv Manuf Technol 72(5) (2014) 653-663.
[63] D. Weller, C. Bezençon, P. Stritt, R. Weber, T. Graf, Remote Laser Welding of Multi-Alloy Aluminum at Close-Edge Position, Physics Procedia 41 (2013) 164-168.
[64] P.K.C. Wood, C.A. Schley, M.A. Williams, A. Rusinek, A model to describe the high rate performance of self-piercing riveted joints in sheet aluminium, Materials & Design 32(4) (2011) 2246-2259.
[65] A. Alshaer, L. Li, A. Mistry, Understanding the effect of heat input and sheet gap on porosity formation in fillet edge and flange couch laser welding of AC-170PX aluminum alloy for automotive component manufacture, Journal of Manufacturing Science and Engineering 137(2) (2015) 021011.
[66] M. Harooni, F. Kong, B. Carlson, R. Kovacevic, Studying the effect of laser welding parameters on the quality of ZEK100 magnesium alloy sheets in lap joint configuration, ICALEO, Laser Institute of America, Anaheim, CA, 2012, pp. 539-548.
[67] W. Meng, Z. Li, J. Huang, Y. Wu, R. Cao, Effect of gap on plasma and molten pool dynamics during laser lap welding for T-joints, Int J Adv Manuf Technol 69(5) (2013) 1105-1112.

[68] ESIS, P7-00 ESIS Procedure for dynamic tensile tests. TC5 Subcommittee on Dynamic Testing at Intermediate Strain rates., 2000.
[69] N. McCormick, J. Lord, Digital Image Correlation, Materials Today 13(12) (2010) 52-54.
[70] GOM, ARAMIS V5.3.0 user manual, 2004.
[71] Y. Chen, A.H. Clausen, O.S. Hopperstad, M. Langseth, Stress–strain behaviour of aluminium alloys at a wide range of strain rates, International Journal of Solids and Structures 46(21) (2009) 3825-3835.
[72] A.H. Clausen, T. Børvik, O.S. Hopperstad, A. Benallal, Flow and fracture characteristics of aluminium alloy AA5083–H116 as function of strain rate, temperature and triaxiality, Materials Science and Engineering: A 364(1) (2004) 260-272.
[73] N. Sotirov, G. Falkinger, F. Grabner, G. Schmid, R. Schneider, R.J. Grant, R. Kelsch, K. Radlmayr, M. Scheerer, C. Reichl, H. Sehrschön, M. Loipetsberger, Improved Formability of AA5182 Aluminium Alloy Sheet at Cryogenic Temperatures, Materials Today: Proceedings 2 (2015) S113-S118.
[74] N.K. Langhelle, J. Amdahl, Experimental And Numerical Analysis of Aluminium Columns Subjected to Fire, The Eleventh International Offshore and Polar Engineering Conference, International Society of Offshore and Polar Engineers, Stavanger, Norway, 2001, p. 8.
[75] J.C. Free, P.T. Summers, B.Y. Lattimer, S.W. Case, Mechanical Properties of 5000 Series Aluminum Alloys Following Fire Exposure, TMS 2016 145th Annual Meeting & Exhibition, Springer International Publishing, Cham, 2016, pp. 657-664.
[76] E.L. Huskins, B. Cao, K.T. Ramesh, Strengthening mechanisms in an Al–Mg alloy, Materials Science and Engineering: A 527(6) (2010) 1292-1298.
[77] X. Sun, M.A. Khaleel, Dynamic strength evaluations for self-piercing rivets and resistance spot welds joining similar and dissimilar metals, International Journal of Impact Engineering 34(10) (2007) 1668-1682.
[78] B. Gurrutxaga-Lerma, D.S. Balint, D. Dini, A.P. Sutton, The mechanisms governing the activation of dislocation sources in aluminum at different strain rates, Journal of the Mechanics and Physics of Solids 84 (2015) 273-292.
[79] H.-P. Wang, C.-T. Wu, Y. Guo, M.E. Botkin, A coupled meshfree/finite element method for automotive crashworthiness simulations, International Journal of Impact Engineering 36(10) (2009) 1210-1222.
[80] L. Papadakis, A. Schober, M.F. Zaeh, Numerical investigation of the influence of preliminary manufacturing processes on the crash behaviour of automotive body assemblies, Int J Adv Manuf Technol 65(5) (2013) 867-880.
[81] J.O.J. Hallquist, LS-DYNA keyword user's manual, Livermore Software Technology Corporation 970 (2007) 299-800.
[82] D. Li, A. Chrysanthou, I. Patel, G. Williams, Self-piercing riveting-a review, Int J Adv Manuf Technol 92(5-8) (2017) 1777-1824.
[83] Henrob, 2018. http://www.henrob.co.uk/. (Accessed 04/12/2018.
[84] C.G. Pickin, K. Young, I. Tuersley, Joining of lightweight sandwich sheets to aluminium using self-pierce riveting, Materials & Design 28(8) (2007) 2361-2365.
[85] M. Kimchi, D.H. Phillips, Resistance spot welding: fundamentals and applications for the automotive industry, Synthesis Lectures on Mechanical Engineering 1(2) (2017) i-115.
[86] H. Eisazadeh, M. Hamedi, A. Halvaee, New parametric study of nugget size in resistance spot welding process using finite element method, Materials & Design 31(1) (2010) 149-157.